AGU PUBLICATIONS

JGR

Journal of Geophysical Research: Oceans

RESEARCH ARTICLE

10.1002/2013JC008979

Key Points:
- Basic physics of internal wave interactions clarified
- Advice given on internally consistent estimates
- Examples of biases discussed

Correspondence to:
K. L. Polzin,
kpolzin@whoi.edu

Citation:
Polzin, K. L., A. C. N. Garabato, T. N. Huussen, B. M. Sloyan, and S. Waterman (2014), Finescale parameterizations of turbulent dissipation, *J. Geophys. Res. Oceans*, *119*, 1383–1419, doi:10.1002/2013JC008979.

Received 1 APR 2013
Accepted 20 DEC 2013
Accepted article online 2 JAN 2014
Published online 25 FEB 2014

Finescale parameterizations of turbulent dissipation

Kurt L. Polzin[1], Alberto C. Naveira Garabato[2], Tycho N. Huussen[3], Bernadette M. Sloyan[4,5], and Stephanie Waterman[6,7,8]

[1]Woods Hole Oceanographic Institution, Woods Hole, Massachusetts, USA, [2]National Oceanographic Centre, Southampton, UK, [3]Scripps Institute of Oceanography, San Diego, California, USA, [4]Center for Australian Weather and Climate, CSIRO, Hobart, Tasmania, Australia, [5]CSIRO Wealth from Ocean National Research Flagship, Hobart, Tasmania, Australia, [6]Australian National University, Sydney, New South Wales, Australia, [7]Department of Earth, Ocean & Atmospheric Sciences, University of British Columbia, Vancouver, BC, Canada, [8]Climate Change Research Centre and ARC Centre of Excellence for Climate System Science, University of New South Wales, Sydney, New South Wales, Australia.

Abstract This article (1) reviews and clarifies the basic physics underpinning finescale parameterizations of turbulent dissipation due to internal wave breaking and (2) provides advice on the implementation of the parameterizations in a way that is most consistent with the underlying physics, with due consideration given to common instrumental issues. Potential biases in the parameterization results are discussed in light of both (1) and (2), and illustrated with examples in the literature. The value of finescale parameterizations for studies of the large-scale ocean circulation in the presence of common biases is assessed. We conclude that the parameterizations can contribute significantly to the resolution of large-scale circulation problems associated with plausible ranges in the rates of turbulent dissipation and diapycnal mixing spanning an order of magnitude or more.

1. Introduction

The use of finescale parameterizations of turbulent dissipation by internal wave breaking, consisting of predictions for the turbulent kinetic energy dissipation rate (ϵ) from internal wave shear and strain on wavelengths of tens to hundreds of meters [*Gregg*, 1989; *Polzin et al.*, 1995], has experienced an explosion in recent years [e.g., *Gregg and Kunze*, 1991; *Kunze et al.*, 1992; *Kunze and Sanford*, 1996; *Mauritzen et al.*, 2002; *Garabato et al.*, 2004a, 2004b; *Sloyan*, 2005; *Walter et al.*, 2005; *Kunze et al.*, 2006; *Alford et al.*, 2007; *Palmer et al.*, 2007; *MacKinnon et al.*, 2008; *Stöber et al.*, 2008; *Lauderdale et al.*, 2008; *Park et al.*, 2008; *Daae et al.*, 2009; *Fer et al.*, 2010; *Wu et al.*, 2011; *Huussen et al.*, 2012; *Whalen et al.*, 2012]. This has been largely motivated by the prospect of gaining insight into the geographical distribution, magnitude and forcing of diapycnal transformations in the ocean as characterized by the diapycnal diffusivity (K_ρ), by applying the parameterizations to density and/or velocity measurements obtained with standard conductivity–temperature-depth (CTD) and Acoustic Doppler Current Profiler (ADCP) instrumentation. These types of data are much more extensive and are easier to obtain than microstructure observations. Since internal wave breaking is widely thought to be a leading order contributor to the diapycnal closure of the ocean's overturning circulation and to the maintenance of the abyssal stratification [e.g., *Wunsch and Ferrari*, 2004], the potential for finescale analyses to drive a step change in our knowledge of important aspects of the ocean mixing problem is significant.

Against this backdrop of a rapidly growing literature, it has become apparent that there are divergent opinions on how the finescale parameterizations should be implemented, how data from different instruments should be treated during implementation, how the resulting dissipation rates should be interpreted, and what the expected uncertainties of these results are. Illustrations of the developing controversy are given by *Kunze et al.* [2006] and *Huussen et al.* [2012], both of whom apply a nominally unique finescale parameterization to a particular data set that results in dissipation rates differing by up to an order of magnitude. It follows that, at present, the usefulness of finescale parameterizations is severely limited by the apparent sensitivity of their outcomes to a range of implementation and interpretation particulars. In this article, we seek to lay a way forward by addressing these issues in a systematic fashion. First, we review the basic physics underpinning finescale parameterizations, bringing together the somewhat obscure theoretical literature with the authors' own insights, and synthesizing this information for a wide physical oceanographic audience. Second, we advise on how finescale parameterizations should be implemented in a way that is

most consistent with the underlying physics while avoiding common instrumental problems. In so doing, we provide specific illustrations of how these problems can impact the interpretation of the data, and focus on possible *biases* that can arise from incorrectly dealing with instrumental issues as well as from physics missing from the finescale parameterizations. Finally, we discuss the relation of parameterized turbulent dissipation and mixing rates to estimates obtained from budget studies of the large-scale ocean circulation, and reflect on the implications of the preceding ideas for the extent of applicability of the finescale parameterizations and the interpretation of their results.

The article is organized as follows. Section 2 reviews the physics underpinning finescale parameterizations. In section 3, we detail how to formulate expressions that may be applied to oceanic data. The implementation of such expressions is discussed in section 4, with emphasis on the limitations of commonly used instrumentation and the biases they can induce in estimating diapycnal mixing rates. In section 5, we apply the parameterizations to specific oceanic data sets to illustrate the limitations of the method and demonstrate common ambiguities of interpretation. The key points of this study are summarized in section 6, which concludes with a discussion of how finescale estimates of turbulent mixing may relate to basin-scale and global-scale calculations of diapycnal water mass transformations.

2. Physical Basis of Finescale Parameterizations

In this section, we review the physical principles of finescale parameterizations to shed light on both the fundamental physics and the assumptions implicit in their derivation. The discussion is categorized in terms of the three distinct length scales at which significant approximations to the exact physical balances are made in deriving the parameterizations.

2.1. Physical Basis at Large Scales

Connecting the outcome of a finescale parameterization to the rate of diapycnal transformation on ocean basin scales, which is often the primary motivation for the use of the parameterizations, involves a fundamental assumption on the physics of diapycnal mixing. To elicit this point, we consider the advection-diffusion buoyancy balance in an isopycnal-diapycnal (strictly, isoneutral-dianeutral) coordinate system [e.g., *McDougall*, 1987]

$$eN^2/g = \alpha\nabla_\perp \cdot K_\rho \nabla_\perp \Theta - \beta\nabla_\perp \cdot K_\rho \nabla_\perp S - K_\parallel [C_b \nabla_\parallel \Theta \cdot \nabla_\parallel \Theta + T_b \nabla_\parallel \Theta \cdot \nabla_\parallel p], \tag{1}$$

where e is the diapycnal velocity, $N = (-\frac{g}{\rho}\frac{\partial \rho}{\partial z})^{1/2}$ is the buoyancy frequency, g is the acceleration due to gravity, ρ is the density, α and β are the thermal expansion and haline contraction coefficients, respectively, K_ρ and $K_\parallel$ represent eddy diffusivity closures for diapycnal and isopycnal fluxes, C_b and T_b are cabbeling and thermobaric parameters associated with nonlinearities in the equation of state (assuming that $K_S = K_\Theta = K_\rho$, i.e., double-diffusive phenomena are neglected), $\nabla_\parallel$ and $\nabla_\perp$ are gradient operators along and across neutral density surfaces, Θ is the conservative temperature, and p is pressure. The notion that finescale parameterizations may be used to estimate diapycnal transformations assumes the first two terms on the right-hand side of (1) dominate the third and fourth.

2.2. Physical Basis at Small Scales

In order to appreciate the simplifications of the exact small-scale (turbulent) physics implicit in finescale parameterizations, consider the equation of conservation of turbulent kinetic energy, $\mathcal{E}$, i.e.,

$$\rho\frac{\partial \mathcal{E}}{\partial t} + \nabla \cdot \overline{p'\mathbf{u}'} + \mathcal{P} = -\rho\epsilon + \mathcal{B} + p\nabla \cdot \mathbf{u}, \tag{2}$$

where $\mathcal{P}$ is the rate of production of turbulent kinetic energy (approximated as $\mathcal{P} \cong \overline{u'w'}\,\bar{u}_z$ in a one-dimensional situation), ϵ denotes the rate of dissipation of turbulent kinetic energy,

$$\mathcal{B} = g\alpha\overline{w'\theta'} - g\beta\overline{w'S'} = -g\overline{w'\rho'} = -g\alpha K_\theta \nabla_\perp \theta + g\beta K_S \nabla_\perp S = \rho_o N^2 K_\rho \quad \text{if } K_\theta = K_S = K_\rho \tag{3}$$

represents the rate of work against gravity done by turbulent buoyancy fluxes, and $\mathbf{u} = (u, v, w)$ is the velocity. In (2), turbulent quantities are represented as primed variables, whereas overbars indicate an average

over the outer scales of turbulence. If the common assumptions of steady, isotropic conditions is made (such that $\rho\partial_t\mathcal{E}=0$ and $\nabla\cdot\overline{p'\mathbf{u}'}=0$), and if it is further presumed that transformations between internal and kinetic energies associated with nonlinearities in the equation of state are negligible (i.e., $p\nabla\cdot\mathbf{u}=0$, which is equivalent to asserting that the last term in the large-scale buoyancy balance in expression (1) can be neglected), (2) approximates to

$$\mathcal{P}\cong-\rho\epsilon+\mathcal{B}, \tag{4}$$

which states that the turbulent production is balanced by the turbulent dissipation and the turbulent buoyancy flux. In high Reynolds number turbulence, for which production scales are much larger than the scales L_k at which the inertial forces of turbulence are balanced by viscosity ν, $L_k^{-1}\propto(\epsilon/\nu^3)^{1/4}$, ϵ further represents the rate of downscale energy transfer within that range of scales.

The correlations at the core of the definition of the turbulent buoyancy flux in (2) are typically small [*Moum*, 1990]. The buoyancy flux $\mathcal{B}$ is thus difficult to estimate directly. Instead, estimation of $\mathcal{B}$ is commonly made indirectly by assuming, following (4), that $\mathcal{P}$ is balanced by ϵ and $\mathcal{B}$ in fixed proportions, such that

$$\mathcal{B}=R_f\mathcal{P}, \tag{5}$$

where R_f is a flux Richardson number. This expression implies that

$$\mathcal{B}=\frac{R_f}{1-R_f}\epsilon, \tag{6}$$

and, if the usual flux-gradient closure is adopted, it follows that

$$K_\rho=\frac{R_f}{1-R_f}\frac{\epsilon}{N^2}. \tag{7}$$

The use of (7) in the localized determination of diapycnal mixing rates from in situ estimates of ϵ is widespread in the oceanographic literature, where the ratio $\frac{R_f}{1-R_f}$ is regularly termed a "mixing efficiency" Γ and taken to have a constant value of $\Gamma\Gamma=0.2$. This choice corresponds to a flux Richardson number of $R_f=0.17$, which is suggested by laboratory studies and direct numerical simulation of stratified shear flows [*Peltier and Caulfield*, 2003]. Note, however, that mixing efficiencies can be quite context dependent. Most notable is the case of convection, for which turbulent production is zero, i.e., $\rho\epsilon=\mathcal{B}$. Double diffusive convection, which exhibits the added complication that $K_\theta\neq K_S$ in (3), and the effect of nonlinearities in the equation of state, which gives rise to $\nabla\cdot\mathbf{u}\neq0$, are also significant exceptions.

We have thus seen that if the turbulent buoyancy flux at small scales is to be linked to the rate of diapycnal transformation at large scales, it has to be parameterized in terms of the turbulent dissipation rate as in (7). Estimating ϵ in situ requires, in principle, the resolution of the scales [O(1 cm)] at which turbulent kinetic energy is being dissipated by molecular viscosity. Since this can only be done with highly specialized platforms and instrumentation (such as microstructure profilers), alternative, less direct approaches are often followed. One such alternative is the Thorpe-scale method [*Thorpe*, 1977], which implicates the resolution of overturns at the outer scales of turbulence (typically smaller than 1 m) and the subsequent use of the available potential energy ($APE=g\overline{\rho'z'}$) in the overturns as a proxy for turbulent production, $\mathcal{P}\propto APE/N$. *Dillon and Park* [1987] find that 90% of the *APE* production is resolved at vertical wavelengths of $L_T/5$, with Thorpe scale $L_T=(z'^2)^{1/2}$ representing the rms vertical displacement in an overturn. Resolution requirements can be inferred from the empirical relation between the Thorpe scale L_T and Ozmidov length $L_o=(\epsilon/N^3)^{1/2}$: $L_T\approx L_o$ [e.g., *Ferron et al.*, 1998].

While relatively assumption free, the Thorpe-scale method is best applied to density profiles obtained with specialized free-falling profilers rather than with wire-lowered instrumentation, as ship heave associated with oceanic swell is communicated to the instrument package via the lowering wire and may thereby trigger a number of sensor response issues (see section 4). A second alternative approach is provided by models of shear instability, which use the available kinetic energy ($AKE=\delta z^2(N^2-S^2R_{ic}^{-1})/96$) in a supercritical event (for which $R_i<R_{ic}$ and $R_i\equiv N^2/S^2$) as a turbulent production proxy after dividing by a characteristic instability time scale, i.e., τ_c : $\mathcal{P}\propto AKE/\tau_c$ [*Kunze et al.*, 1990; *Polzin*, 1996], giving

$$\epsilon \propto \frac{\delta z^2}{96}(N^2 - S^2 R_{ic}^{-1})\left(N - \sqrt{S^2 R_{ic}^{-1}}\right). \tag{8}$$

The constant of proportionality can be estimated from Figure 5 of *Polzin* [1996]. Again, this method is not well suited for application to routinely acquired physical oceanographic measurements, as it requires resolution of vertical scales δz such that the shear variance $\overline{S^2}$ exceeds approximately $1.1\overline{N^2}$ and requires collocated estimates of N^2 and S^2 [*Polzin*, 1996].

It is the inability of mainstream oceanographic platforms and instrumentation to resolve density and velocity fluctuations on the scales implicated in the Thorpe scale and shear instability approaches that motivates the widespread use of finescale parameterizations. These parameterizations operate on the intermediate [$O(10-100)$m] vertical wavelengths that are generally thought to mediate energy transfers between large and small scales in the ocean, and are much more assumption-dependent than the preceding indirect approaches. The specifics of the approximations implicit in finescale parameterizations are discussed in the following.

2.3. Physical Basis at Intermediate Scales

The physical tenet at the core of finescale parameterizations is that turbulent dissipation at small scales is the end result of a downscale energy transfer driven by nonlinear internal wave-wave interactions. Within this context, the parameterizations seek to relate turbulent dissipation to nonlinearity in the internal wavefield, bypassing the outer scales of turbulence associated with wave breaking and turbulent overturning, which are difficult to measure. This forces the discussion into the spectral domain. In what follows below, $\mathcal{N} = E/\omega$ is the action spectrum; $E = E_k + E_p$ is the energy density; E_k and E_p are the kinetic and potential components of the energy density; ω is the intrinsic frequency; $\mathbf{p} = (k, l, m)$ is the wave number, whose projection onto the horizontal plane (k, l) has modulus $k_h = (k^2 + l^2)^{1/2}$ and horizontal azimuth $\varphi = \tan^{-1}(l/k)$; $\mathbf{C_g} = \nabla_\mathbf{p}\omega$ is the group velocity; $\overline{\mathbf{u}}$ is the velocity on scales larger than $\mathbf{p}^{-1}$; and $\mathcal{R} = d\mathbf{p}/dt$ denotes the rate of change of wave number along a ray as a result of refractive effects in spatially inhomogeneous stratification and larger-scale flows. The spatial coordinate is denoted as $\mathbf{r}$. The factors $\nabla_\mathbf{r}$ and $\nabla_\mathbf{p}$ are gradient operators in the spatial and spectral domains, respectively. The explicit arguments of E will denote its dimensionality, i.e., $E(\omega)$ will be a one-dimensional frequency spectrum, $E(m, \omega)$ will be a two-dimensional vertical wave number-frequency spectrum, etc. The spatial and temporal dependencies of E will not be shown explicitly for clarity of presentation.

2.3.1. Energetics

We start by writing an equation for the energy density of the internal wavefield [*Polzin*, 2004a]:

$$\frac{\partial E_\mathbf{p}}{\partial t} + \nabla_\mathbf{r} \cdot (\mathbf{C_g} + \overline{\mathbf{u}})E_\mathbf{p} + \nabla_\mathbf{p} \cdot \mathcal{R}E_\mathbf{p} = T_r + S_o - S_i, \tag{9}$$

where T_r is the rate of spectral energy transfer due to nonlinearity; S_o is the rate of energy production by interior sources; and S_i is the rate of energy dissipation by interior sinks.

Equation (9) attempts to be a synthesis of wave dynamics in the spectral domain, a schematic map of which is shown in Figure 1. By reference to this expression, several significant approximations implicit in finescale parameterizations may be made explicit. Thus, the parameterizations assume that the internal wavefield is stationary and homogeneous (such that the left-hand side of (9) may be set to zero) and that internal wave sources S_o may be neglected. Equation (9) then simplifies to

$$T_r = S_i. \tag{10}$$

If the dissipation of the internal wavefield occurs through wave breaking and turbulent overturning, as indicated in Figure 1, it follows that the rate of turbulent production must match the wavefield's energy dissipation rate, i.e., $\mathcal{P} = -\int S_i d\mathbf{p}$. This implies, invoking (10), that the rate of nonlinear energy transfer in the wavefield must be balanced by the rate of turbulent production,

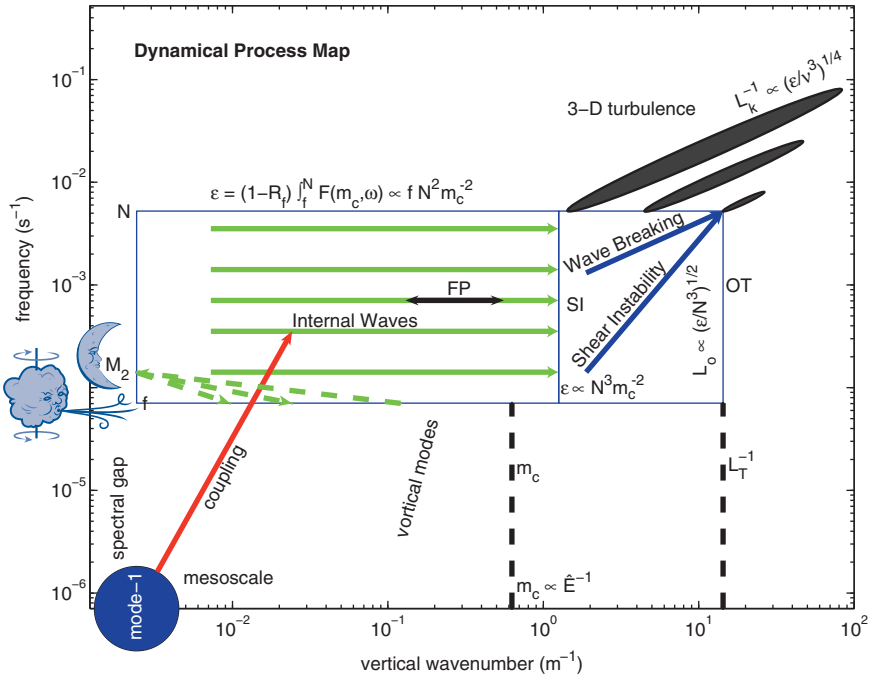

Figure 1. A map of dynamical processes in the vertical wave number—frequency domain. Red colors represent sources associated with wave mean effects, green nonlinear transfers, and blue sinks associated with shear instability and wave breaking. Arrows denote the dominant direction of energy transfer. Nonlinear transfers in the frequency domain are uncertain. Wind forcing and barotropic tidal conversion are regarded here as boundary conditions on the radiation balance equation. The ellipses depict the range of overturning scales for GM, $\sqrt{10}$ and 10 times GM finescale spectral levels. The range of vertical scales for the most robust application of finescale parameterizations (FP), shear instability (SI), and Thorpe-scale (OT) parameterizations of turbulent dissipation are indicated for the GM spectral level, as are the nominal scalings of ϵ, L_T, L_o, and L_k upon m_c, f, and N.

$$\int T_r d\mathbf{p} = \mathcal{P} = -\rho\epsilon + B, \tag{11}$$

where (4) has been used and the integration is carried out to the boundaries of the wave breaking process (8). Expression (11) encapsulates the basic concept underpinning finescale parameterizations: that the rate of turbulent dissipation and the turbulent buoyancy flux occurring at small scales can be inferred from knowledge of the nonlinear energy transfers in the internal wavefield at intermediate scales. We now discuss the next building block of finescale parameterizations, which concerns how T_r may be represented in terms of easily measurable variables and the approximations implicit in that representation.

2.3.2. Dynamics

While the focus is on the energetics of mixing, the dynamics of conservative wave propagation concerns action $\mathcal{N}$, defined as $\mathcal{N} = E/\omega$. Here theoretical estimates of a net downscale transport of action are available from a number of sources.

The first source is a general paradigm of weakly interacting dispersive waves in continuous media referred to as wave turbulence [*Zakharov et al*., 1992; *Nazarenko*, 2011]. One of the corner stones of wave turbulence is the development of kinetic equations quantifying the spectral energy transfer associated with resonant wave interactions for statistically homogeneous systems. In this approach, energy exchange occurs between three waves which are each solutions to the linear problem, see *Müller et al*. [1986] and *Polzin and Lvov* [2011] for discussion of the internal wave problem.

This first principles approach, though, has issues. First, numerical evaluations of the internal wave kinetic equation [*Polzin and Lvov*, 2011] reveal an *O*(1) evolution of the spectrum on time scales of a wave period, contradicting any notion of weak nonlinearity. Second, this approach predicts *no* transfer of energy to smaller vertical scales at high frequency for what is the "universal" Garrett and Munk vertical wave number spectrum, contradicting the common acceptance that the "universal" spectrum defines background mixing rates. Third, for vertical wave number spectra that deviate from the "universal" model, the absence of

transfers in horizontal wave number is problematic as it further requires a source of wave energy at high frequency that has not been observed [*Polzin and Lvov*, 2011].

A second source of theoretical guidance is provided by tracking wave packets in stochastic backgrounds modeled upon the GM spectrum. Ray tracing assumes a scale separation and employs a dispersion relation defined in an infinitesimal amplitude limit. No assumption, though, is made upon the rate of energy transfer between waves that is inherently problematic in the kinetic equation. Here again, there are issues with the first principles approach. As we will see more clearly in section 2.3.4, the assumption of a scale separation is contradicted by numerical results indicating significant transports associated with background waves of similar vertical scale.

2.3.3. A Cascade Representation of the Spectral Energy Transfer Due to Nonlinearity, T_r

The context for the Finescale Parameterization is a finite amplitude and likely strongly interacting limit, with the caveat that the transition to such a strong interaction paradigm is *not* well understood. In this intellectual void, a cascade representation of the spectral energy transfer due to nonlinearity, T_r, may be arrived at through a combination of dimensional analysis and heuristic arguments [*Polzin*, 2004a]. For the purpose of this article, it suffices to say that the end result of that work is the following representation of T_r:

$$T_r \rightarrow \frac{\partial F(m,\omega,\varphi)}{\partial m} + \frac{\partial G(m,\omega,\varphi)}{\partial \omega}, \tag{12}$$

where

$$F(m,\omega,\varphi) = AmN^{-1}\phi(\omega)E(m,\omega,\varphi) \;\; m^3E(m) \tag{13}$$

is the spectral energy transport in the vertical wave number domain, and $G(m,\omega,\varphi)$ is the spectral energy transport in the frequency domain. In expression (13),

$$\phi(\omega) = k_h/m = [(\omega^2 - f^2)/(N^2 - \omega^2)]^{1/2},$$

and the nondimensional constant A is

$$A = 0.20.$$

The functional representation of G is, for all intents and purposes, immaterial. Observations discussed in *Polzin* [2004a] guide us to the result that $G \cong 0$.

The formulation (13) does not attempt to be a general representation of nonlinear transports. It simply summarizes the basic observational patterns. Nonetheless, it is consistent with an action conservation principle. See Appendix A for details.

Equation (9) may be integrated over frequency and horizontal azimuth. After applying no-flux boundary conditions to $G(m,\omega,\varphi)$ [i.e., $G(m,f,\varphi) = G(m,N,\varphi) = 0$], one obtains the expression

$$\int\int F(m,\omega,\varphi)d\omega d\varphi = F(m) \rightarrow \mathcal{P} \tag{14}$$

in an inertial energy cascade (i.e., a transport through the range of wave numbers where internal wave energy is neither produced nor dissipated). Expression (14) states that the rate of turbulent production (and, invoking (4), the rates of turbulent dissipation and diapycnal mixing) is determined by the spectral energy transport in the vertical wave number domain of the internal wavefield. This exercise in dimensional analysis and heuristic arguments becomes highly relevant in the context of the ray tracing model described below.

2.3.4. A Ray Tracing Prescription for $F(m,\omega)$

In the context of ray tracing techniques, the energy transport can be represented as [*Henyey et al.*, 1986]

$$F(m,\omega) = \; < E(m,\omega) \;\; \frac{dm}{dt} >, \tag{15}$$

where $dm/dt = -(kU_z + lV_z)$ is the temporal evolution of a single wave packet's vertical wave number in response to inertial frequency vertical shear. The factor dm/dt represents the vertical component of the rate

of refraction $\mathcal{R}=-\nabla_{\mathbf{r}}(\omega+\mathbf{p}\cdot\bar{\mathbf{u}})$ for this inertial frequency, larger-scale background flow characterized by vertical shear $(U_z,\ V_z)$. The angled brackets indicate an average over a large number of wave packets. Equation (15) states that the average spectral transport associated with wave packets of wave number **p**, frequency ω and energy density $E(\mathbf{p})$ occurs at a rate dm/dt. For ease of interpretation, this spectral transport may be likened to an average particle flux, with $E(\mathbf{p})$ denoting particle size and *dm/dt* particle velocity across vertical wave number space. We remark that *F* must be defined as an average over many wave packets (particles): energy may be transported toward higher or lower vertical wave numbers for any individual wave packet, and it is only the average transfer for a large set of packets that must be directed downscale.

Assuming no correlation between the energy density and the rate of change of vertical wave number in (15), *Henyey et al*. [1986] obtain

$$F(m,\omega)=E(m,\omega)<\frac{dm}{dt}>=E(m,\omega)k_hS(m)C(m)/\sqrt{2}, \tag{16}$$

where $S(m)$ is the rms shear, defined via

$$S^2(m)=\int_0^m 2m'^2E_k(m')dm', \tag{17}$$

and $E_k(m)$ denotes the kinetic energy density. The factor $C(m)$ is expressed as $[1-r(m)]/[1+r(m)]$ by *Henyey et al*. [1986], with $r(m)$ indicating the ratio of the spectral energy transports toward higher and lower vertical wave numbers. Those authors apply Monte Carlo techniques to the ray-tracing results in order to estimate $r(m)$ at an upper wave number m_u beyond which the test waves are considered to break.

The key step in developing a general parameterization [*Polzin et al*., 1995] is to realize that test-wave spectra [*Flatté et al*., 1985] are consistent with the GM76 (the 1976 version of the Garrett and Munk spectrum, see *Polzin and Lvov* [2011] for discussion of that model and its variants) vertical wave number spectrum representing a stationary state. The functional dependence of $C(m)\propto S(m)/N$ reproduces this tendency and (16) may thus be rewritten as [*Polzin et al*., 1995]

$$F(m,\omega)=AmN^{-1}\phi(\omega)E(m,\omega)\int_0^m 2m'^2E_k(m')dm', \tag{18}$$

where the previously defined factor *A* is a product of several constants within the *Henyey et al*. [1986] formulation, and $\phi(\omega)$, also defined above, denotes the ratio between the horizontal and vertical wave numbers implied by a linear internal wave dispersion relation.

The finescale parameterization is *not* a parameterization of near-inertial wave breaking. Rather, it is a parameterization of the net effects of near-inertial oscillations in transporting the energy associated with high-frequency waves to dissipation scales. High-frequency, small-scale waves provide the direct link to mixing. The role of high frequencies in creating dissipation can be appreciated by approximating $F(m,\omega)\propto 1/\omega$, so that the total transport $F(m)=\int_f^N F(m,\omega)d\omega\propto \ln(\omega)|_f^N=\ln(\frac{N}{f})=\ln(\frac{2f}{f})+\ln(\frac{N}{2f})$, in which the direct contribution of near-inertial waves to the total transport is inconsequential: ln(2) $\ll$ ln(N/2f).

Note that, since the integral in (18) is dominated by contributions from vertical wave numbers $m'\cong m$ (i.e., $\int_0^m m'^2E_k(m')dm'\cong m^3E_k(m)$), expression (18) is in essence a *local* closure for *F* in the vertical wave number domain. This fact can be used to further simplify (18) to

$$F(m,\omega)=2Am^4N^{-1}\phi(\omega)E(m,\omega)E_k(m). \tag{19}$$

Note the tension between this result and the assumption of a scale separation required in the derivation of the action balance (Appendix A) and the similarity between (13) and (19). The ray tracing model employs a suspect scale separation assumption that brings into question the validity of the basic action balance and uses a dispersion relation defined in a problematic small amplitude limit. Yet one can obtain a similar result via dimensional analysis and observational (heuristic) constraints.

Jointly with (4) and (14), (18) or (19) forms the basis of finescale parameterizations of turbulent dissipation and diapycnal mixing by internal wave breaking. This set of three equations relates the rates of dissipation and mixing to the energy density of the internal wavefield, the ambient stratification, and the wave field's aspect ratio (represented by $\phi(\omega)$). In section 3, we will describe how (18) and (19) are used to estimate ϵ and K_ρ in practice. Prior to this, we summarize the main approximations to the exact intermediate-scale physics that are involved in the derivation of (18) and (19), and comment on the limitations they impose on the accuracy of the estimated dissipation and mixing rates.

2.3.5. Limitations

We have shown that two of the three expressions at the core of finescale parameterizations ((14), and (18)–(19)) originate from a radiation balance equation (9) describing the evolution of the internal wave field's energy under the influence of a range of processes, namely: time dependence, wave propagation, wave-mean interactions, refraction by a spatially inhomogeneous medium, nonlinearity, forcing and wave breaking, which ultimately leads to turbulent dissipation and mixing by three-dimensional turbulence (see Figure 1). The approximations made in the derivation of (14) and (18)–(19) assert, in essence, that the rate of turbulent dissipation (i.e., ϵ) is proportional (by a factor $(1-R_f)$) to the rate of downscale energy transfer due to nonlinearity (i.e., $F(m,\omega)$) evaluated over the domains $[0 < m < m_c]$ and $[f < \omega < N]$, with m_c a high wave number limit representing a transition into wave-breaking phenomena. This dynamical transition is not precisely defined, but the observed spectral transition where the shear variance exceeds $2\pi N^2/10$,

$$S^2(m_c) \equiv \int_0^{m_c} 2m'^2 E_k(m')dm' \equiv 2\pi N^2/10. \tag{20}$$

serves as a pragmatic definition for m_c. Below, we discuss the set of oceanic conditions under which these approximations are likely to hold or otherwise.

While there are limitations on applying finescale parameterizations to small scales, there are also limitations at large scales. Implicit in (18) and (19) is the notion that waves of vertical wave number m_c are produced locally (in space and time). The issue of spatiotemporal locality is rendered more concrete by considering the ratio of time scales characterizing nonlinearity (τ_{nlin}) and linear wave propagation (τ_{lin}) for an arbitrary vertical wave number and frequency. The ratio of the two time scales may be expressed as

$$\frac{\tau_{nlin}}{\tau_{lin}} = \frac{2\pi}{\omega}\frac{\partial_t E}{\partial_m F} \cong \frac{\omega}{2\pi}\frac{mE(m,\omega)}{F(m,\omega)} \cong \frac{2\omega}{(\omega^2-f^2)^{1/2}}\frac{m_c}{m}. \tag{21}$$

This shows that for vertical wave numbers close to m_c the ratio of time scales is $O(1)$ for a wide range of frequencies, and therefore that nonlinear transports are sufficiently vigorous to remove the energy resident near a vertical wave number m_c in several wave periods. Note, for reference, that hydrostatic nonrotating internal waves typically propagate one wavelength in one wave period, and that waves affected by rotation are even slower, such that the locality assumption above is endorsed. At larger vertical scales ($m \ll m_c$), the identification of downscale transports with turbulent production (18)-(19) is increasingly problematic due to the *possible* contribution of other effects in (9) such as wave-mean interactions.

In order to gauge the extent to which wave-mean interactions may be significant, it is convenient to evaluate the ratio of time scales characterizing wave-wave and wave-mean interactions. Invoking the ray tracing equations and assuming waves are randomly aligned with the mean shear, the ratio can be shown to be

$$\frac{\tau_{nlin}}{\tau_{wm}} = \frac{dm/dt_{\text{wave}-\text{mean}}}{dm/dt_{\text{wave}-\text{wave}}} = \frac{k_h \bar{u}_z}{k_h S(m) C(m)} \cong 8\frac{\bar{u}_z}{N}\frac{m_c}{m}. \tag{22}$$

Equation (22) states that, if the waves are randomly aligned with the mean shear, wave-mean interactions dominate the spectral energy transport in vertical wave number space at m_c for mean shears in excess of $N/8$. The critical mean shear above which wave-mean interactions become significant is even smaller ($N/8\sqrt{2}$) for waves that are aligned with the mean shear. In contrast, the impact of the mean shear on waves propagating normal to the geostrophic velocity is limited to the modification of the ambient vorticity

by the relative vorticity of the mean flow [*Kunze*, 1985; *Polzin*, 2008]. Froude numbers $Fr=\bar{u}_z/N$ in excess of 0.1 are often characteristic of upper-ocean fronts, equatorial current systems and topographic Rossby waves. Applications of finescale parameterizations in such situations should be regarded as problematic. However, tests in an upper ocean front [*Polzin et al*., 1996a], a warm core ring [*Polzin et al*., 1995], and the Florida Current [*Winkel et al*., 2002; *Gregg et al*., 2003] have not suggested significant discrepancies. In the first two instances, it is understood that the finescale wavefield tends to be aligned normal to the thermal wind shear.

The central assumption of expressions (18) and (19), i.e., that the downscale energy transport toward the scales of turbulent production is driven by nonlinearity in the internal wave field, may also be violated by boundary conditions. The nonlinear downscale energy transfer past $m=m_c$ may be short-circuited by internal wave scattering [*Müller and Xu*, 1992] and reflection [*Eriksen*, 1985] at a boundary transferring energy between very different scales, expressed as the insertion of significant shear at scales smaller than $1/m_c$ near the boundary. *Kunze et al*. [2002] and *Gregg et al*. [2005] infer very poor agreement between (19) and observations from Monterey Canyon. Since *Kunze et al*. [2002] infer $2\pi/m_c$ is larger than the total water column depth for their more energetic profiles, the data may not be sufficiently far from forcing and boundaries. We return to this interpretation in section 5. Regardless, the finescale parameterization should not be expected to work well if wave generation inserts significant shear into vertical scales smaller than $1/m_c$. Failure of finescale parameterizations should also be anticipated in boundary layers where dissipation is associated with viscous stresses, as that process is not accounted for in the parameterizations.

Finescale parameterizations are not intended to be an all-inclusive summary of internal wave-wave interactions. They are based on ray-tracing simulations of test waves propagating in a broadband wavefield at finite amplitude. Formulae for the downscale energy transport associated with infinitesimal amplitude waves in the resonant interaction approximation [*McComas and Müller*, 1981] provide essentially the same prediction for ϵ [*Polzin*, 2004a], and thus (18) and (19) appear as relatively generic expressions. However, despite this degree of generality, finescale parameterizations are *not* designed to capture spectral energy transports in narrow-band wavefields, such as that associated with the parametric subharmonic instability (PSI) of a mode-1 internal tide.

To recapitulate, there is a plethora of factors that might lead to error in the outcomes of finestructure parameterizations, specifically:

1. nonlocal spectral transports associated with wave breaking (e.g., shear instability);

2. competition with wave-mean driven spectral transports;

3. boundary conditions short-circuiting the downscale energy transfer;

4. nonlocal spectral transports associated with resonant interactions;

5. stress-driven boundary layers.

Considering these, it is rather remarkable that finescale parameterizations perform as well as they will be shown to do later in this article.

3. Formulation of Finescale Parameterizations

We have shown above that the physical basis of finescale parameterizations can be synthesized in expressions (4), (14) and (18) or (19). In this section, we derive the formulation of finescale parameterizations from those expressions, and discuss the approximations implicit in the derivation.

3.1. An Estimate of the Spectral Energy Transport in the Vertical Wave Number Domain, *F*, for the GM Internal Wave Spectrum

For reasons of convenience, finescale parameterizations are formulated by reference to the GM internal wave spectrum rather than directly using (18) and (19). It is thus instructive to commence our derivation of the finescale parameterization formulae by calculating the rate of turbulent production, $\mathcal{P}$, or equivalently (through (14)), the spectral energy transport in the vertical wave number domain, F, for the GM canonical internal wave field.

The energy density for the GM76 internal wave spectrum is [*Polzin and Lvov*, 2011]

$$E(m,\omega)=\frac{N}{N_o}E_o\frac{2f}{\pi}\frac{1}{\omega\sqrt{\omega^2-f^2}}\frac{2}{\pi}\frac{m_*}{m_*^2+m^2}, \tag{23}$$

where $N_o=3$ cph, $E_o=3.0\times10^{-3}$ m^2 s^{-2}, $m_*=m_oN/N_o$, and $m_o=4\pi/1300$ m. The equivalent mode number m_* has been changed from 3 to 4 so that (23) has the same total energy E_o and high-wave number asymptote, $m^2/(m_*^2+m^2)$, as the nominal GM76 model. Using the kinematic relations for linear internal waves, (23) yields

$$m^2E_k(m)=m^2\int_f^N\frac{\omega^2+f^2}{2\omega^2}\frac{2f}{\pi}\frac{1}{\omega\sqrt{\omega^2-f^2}}E(m)d\omega\cong\frac{3}{4}m^2E(m), \tag{24}$$

which is equivalent to stating that the ratio of kinetic and potential energy densities for the GM spectrum is $E_k(m)/E_p(m)=3$. Substituting (24) into (18) and integrating over internal wave frequencies, we obtain the following estimate for the spectral energy transport in the vertical wave number domain,

$$F(m)=\int_f^N F(m,\omega)d\omega\cong\frac{3Af}{\pi N^2}\cosh^{-1}\left[\frac{N}{f}\right]\ mE(m)\int_0^m m'^2E(m')dm', \tag{25}$$

where

$$E_o^{-1}\int_f^N\left[\frac{\omega^2-f^2}{N^2-\omega^2}\right]^{1/2}E(\omega)d\omega=\int_f^N\left[\frac{\omega^2-f^2}{N^2-\omega^2}\right]^{1/2}\frac{2f}{\pi}\frac{1}{\omega\sqrt{\omega^2-f^2}}d\omega\cong\frac{2f}{\pi N}\cosh^{-1}\left[\frac{N}{f}\right] \tag{26}$$

has been used. Taking the high vertical wave number asymptotic limit, $m\gg m_*$, we obtain

$$F(m)\rightarrow\frac{6f}{10\pi}\cosh^{-1}\left[\frac{N}{f}\right]\frac{E_o^2}{N_o^2}\left[\frac{2}{\pi}\right]^2\frac{m_o^2N^2}{N_o^2}\propto fN^2E_o^2, \tag{27}$$

which yields $F(m)=8\times10^{-10}$ W kg^{-1} at a latitude of 32.5° and for $N=3$ cph. This estimate of the spectral energy transport in the vertical wave number domain for the GM spectrum is at the core of the formulation of finescale parameterizations. The remaining components of the parameterization algorithm are introduced next.

3.2. A Parameterization Algorithm for Non-GM Conditions

The formulation of finescale parameterizations by reference to the GM internal wave spectrum demands care in treating deviations from the GM model. This is because the finescale observations to which the parameterizations are typically applied provide only incomplete information on the 2-D vertical wave number-frequency spectrum, such that evaluation of $E(m,\omega)$ in (18) and (19) is not possible. To deal with this limitation, several simplifications are made to (18) and (19). Approximations in the vertical wave number and frequency domains are discussed separately below.

3.2.1. Approximations in the Frequency Domain

As indicated by (19), an algorithm to estimate the downscale energy transport contains two frequency-dependent corrections. The first correction results from the integration of the frequency-dependent elements of (19) over the internal wave frequency band,

$$\bar{\phi}\equiv\frac{\int_f^N\phi(\omega)E(\omega,m_c)d\omega}{\int_f^N E(\omega,m_c)d\omega}=\frac{\int_f^N\left[\frac{\omega^2-f^2}{N^2-\omega^2}\right]^{1/2}E(\omega,m_c)d\omega}{E(m_c)}, \tag{28}$$

and represents an energy density weighted estimate of the mean aspect ratio of the internal wave field, $\phi(\omega)=[\frac{\omega^2-f^2}{N^2-\omega^2}]^{1/2}$. The factor $E(\omega,m_c)$ is the frequency spectrum of the energy density at $m=m_c$.

In the absence of observations of $E(\omega, m_c)$, as relevant to the common case of coarse temporal sampling, the only available source of information on the frequency content of the wave field is the ratio of horizontal kinetic and potential energies R_ω (also known as the shear-to-strain ratio). For a *single* frequency,

$$\begin{aligned} R_\omega &\equiv \frac{E_k}{E_p} = \frac{2m^2 E_k}{2m^2 E_p} \\ &= \frac{\omega^2+f^2}{\omega^2-f^2}\frac{N^2-\omega^2}{N^2} \\ &\cong \frac{\omega^2+f^2}{\omega^2-f^2}, \end{aligned} \tag{29}$$

where the hydrostatic approximation has been applied in the last equality. A little algebra returns the single wave relation for the aspect ratio,

$$\begin{aligned} \phi(\omega) &= \frac{k_h}{m} \\ &= \left[\frac{\omega^2-f^2}{N^2-\omega^2}\right]^{1/2} \\ &= \left[\frac{-R_\omega+1+\frac{f^2}{N^2}+\left[\left(R_\omega-1-\frac{f^2}{N^2}\right)^2+8R_\omega\frac{f^2}{N^2}\right]^{1/2}}{2R_\omega}\right]^{1/2} \\ &\cong \frac{f}{N}\left[\frac{2}{R_\omega-1}\right]^{1/2}, \end{aligned} \tag{30}$$

where the last equality again represents the hydrostatic approximation. The single wave relation (30) is a biased estimator of the multiwave spectral representation of $\phi(\omega)$ in (28). A sense of the bias can be obtained from Figure A1 of *Polzin et al*. [1995].

The second frequency-related correction is more trivial, and links the total and kinetic energy densities. Specifically, after integrating in the frequency domain, $F(m_c)$ contains a factor of $E(m_c)=E_k(m_c)+E_p(m_c)=E_k(m_c)\frac{R_\omega+1}{R_\omega}$. As indicated by (24), the GM internal wave field has $E(m_c)=\frac{4}{3}E_k(m_c)$.

3.2.2. Approximations in the Vertical Wave Number Domain

The amplitude factor in (18), $mE(m)\int_0^m m'^2\, E_k(m')dm'$, consists of two different moments of the vertical wave number spectrum. If sampling is sufficient to obtain smooth spectra, (18) can be directly evaluated. This has not hitherto been done. Rather, the amplitude factor has been approximated as

$$\begin{aligned} F(m) &\propto mE(m)\int_0^m m'^2 E_k(m')dm' \\ &\cong \frac{R_\omega+1}{R_\omega}[m^2E_k(m)]^2. \end{aligned} \tag{31}$$

The amplitude factor on the right-hand side of (31) is nearly independent of vertical wave number and consequently averaging in vertical wave number can decrease the statistical uncertainty. If the spectra are resolved to m_c,

$$\begin{aligned} <[2m^2E_k(m)]>^2 &= \left[\frac{1}{m_c}\int_0^{m_c} 2m'^2E_k(m')dm'\right]^2 \\ &\equiv \left[\frac{2\pi N^2}{10m_c}\right]^2. \end{aligned} \tag{32}$$

It is convenient to express (32) in terms of a nondimensional gradient spectral level $\hat{E}$:

$$\hat{E}(m_c) = \frac{0.1\text{cpm}}{m_c}, \tag{33}$$

as represented in *Polzin et al*. [1995].

The decrease in statistical uncertainty, however, is at the cost of a potential bias. Assuming a functional form of $E(m) = am^{-(2+p)}$, the left-hand side of (31) evaluates as

$$F(m_c) \propto (1-p)\left[\frac{2\pi N^2}{10 m_c}\right]^2, \tag{34}$$

so that (32) is a biased estimator of $F(m_c)$ by a factor of $(1-p)$. The approximation contained in (31) is exact if the shear spectrum is white ($p = 0$) and the issue of bias inherent in (31) only affects non-GM spectra.

3.2.2.1. Lack of Resolution

Further intricacies are introduced when the instrumentation does not resolve m_c and the parameterizations are applied to individual profiles, for which spectral transport estimates via (18) and (19) can be quite noisy. In practice, one can estimate $\hat{E}$ and R_ω via (32), replacing the integration bounds of $(0, m_c)$ with (m_1, m_2) to estimate the average shear and strain spectral density in the vertical wave number band (m_1, m_2) and normalizing by the GM76 shear spectrum's high wave number asymptote of $2\pi N^2/10 m_c$

$$\hat{E} = \frac{\left[\frac{1}{m_2-m_1}\int_{m_1}^{m_2} 2m'^2 E_k(m')dm'\right]}{2\pi N^2/10 m_c}. \tag{35}$$

The bias is relatively small for the GM spectrum: estimates of $F(m,\omega)$ via (35) differ from (18) by less than 5% if $(m_1, m_2) = (0, m_c)$ and by less than 25% if $(m_1, m_2) = (0, m_c/10)$. An alternative is the GM76 spectral density resident in the chosen wave number band,

$$\hat{E} = \frac{\left[\frac{1}{m_2-m_1}\int_{m_1}^{m_2} m'^2 E_k(m')dm'\right]}{\left[\frac{1}{m_2-m_1}\int_{m_1}^{m_2} m'^2 E_k^{GM}(m')dm'\right]}. \tag{36}$$

Definition (36), though, is entirely ad hoc as the transport $F(m)$ associated with the GM76 spectrum is independent of m only in the limit $m \gg m_*$. Use of (35) rather than (36) avoids possible bias incurred if the GM75 functional form of $E(m) \propto 1/(m_* + m)^2$ is used rather than the GM76 form, $E(m) \propto 1/(m_*^2 + m^2)$. The distinction is that $1/(m_*^2 + m^2)$ reaches its asymptotic $1/m^2$ dependence much more rapidly than $1/(m_* + m)^2$ and the dissipation is defined as the asymptotic limit (27). A factor of two bias is possible using GM75 at thermocline stratification rates if only vertical wavelengths larger than 100 m are resolved.

Issues of bias become considerably more problematic as the spectrum departs significantly from that of the GM prescription. The degree of bias inherent in (35) is a function of both the bandwidth m_o (23) in relation to the resolved wave number band $m_1 \le m \le m_2$ and of the characteristic slope of the shear spectrum, Figure 2. Here we have considered a parametric representation for the energy spectrum of the form:

$$E(m) \propto (m_o^2 + m^2)^{-p/2}, \tag{37}$$

normalized the spectra so that $m_c = 0.1$ cpm and evaluated the bias as

$$\frac{\left[\frac{1}{m_2-m_1}\int_{m_1}^{m_2} m'^2 E_k(m')dm'\right]^2}{m_c E(m_c)\int_0^{m_c} m'^2 E(m'dm')}. \tag{38}$$

The bias, both underestimates and overestimates, can exceed an order of magnitude, Figure 2. To infer the significance of such biases, one needs to know a global distribution of m_o and high-wave number power

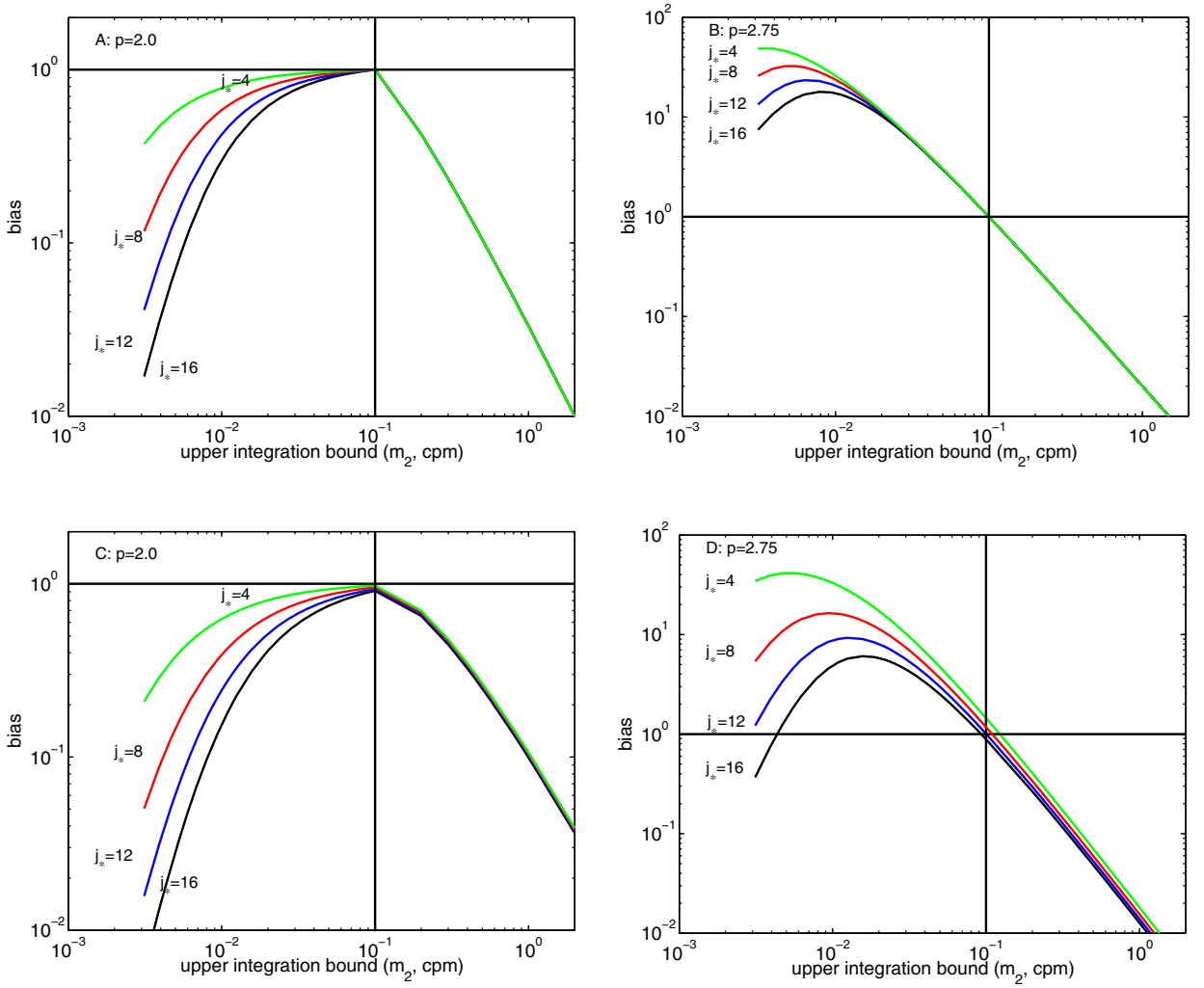

Figure 2. (top) Finescale dissipation bias $F(m_2)/F(m_c)$ associated with evaluating (18) at wave number $m_2 \neq m_c$ as a function of spectral bandwidth m_o given as equivalent mode number j_* in the figures. (a) $p = 2$ and (b) p=2.75 with p representing the power law of the vertical wave number energy spectrum. (bottom) Finescale dissipation bias (38) associated with approximating (18) using (35) and evaluating the shear spectral density over wave numbers $(0, m_2)$. (c) $p = 2$ and (d) p=2.75. The spectra have been normalized so that m_c=0.1 cpm.

laws, which we do *not* have access to. The catalogue in *Polzin and Lvov* [2011] suggests that low bandwidths occur in combination with relatively white (GM power law) shear spectra, and that large bandwidths occur in conjunction with shear spectra steeper than GM. Such covariability will tend to exclude the extreme values of possible biasing in Figure 2, but it is difficult to argue this point with confidence without having fully resolved shear spectra.

In choosing a wave number band, there is thus much to be gained from resolving small scales in order to avoid biasing $\hat{E}$. However, there is also a premium with regards to avoiding noise, section 4.2. Concrete examples of this trade-off are given in section 5.

3.2.2.2. Insufficient Bandwidth With Sufficient Resolution

There are relevant cases in which one can take too small a transform length in the spectral analysis implicit in the estimation of $\hat{E}$. Choosing too large a value for m_1 may result in m_2 being significantly larger than m_c if the integration is carried out to obtain a shear variance of $2\pi N^2/10$. Assuming a functional form in which the gradient spectra are white for $0 < m < m_c$ and roll-off as m_c/m at higher wave number, the estimate of $\hat{E}$ will be biased:

$$\frac{\left[\frac{1}{m_2-m_1}\int_{m_1}^{m_2} 2m'^2 E_k(m')dm'\right]}{2\pi N^2/10m_c} = \frac{1}{\exp(m_1/m_c)-(m_1/m_c)} \quad . \tag{39}$$

If $m_1 = m_c$, the estimate of turbulent production is biased low by a factor 0.34.

3.2.2.3. Indiscriminate Hyper-resolution

The finescale parameterization does not apply at vertical wave numbers in excess of m_c, as that domain is dominated by transfers associated with wave breaking and strongly nonlinear effects. Including vertical wave numbers in excess of m_c can lead to a significant bias [*Gargett*, 1990]. We illustrate this effect by including $m_2 \gg m_c$ in our estimates of bias, Figure 2. Biases in excess of an order of magnitude are possible.

3.3. Formulation

Finally, we arrive at the finescale parameterization formula for the rate of turbulent production estimated from vertical profile measurements:

$$\mathcal{P} = 8\times10^{-10}\frac{f}{f_o}\frac{N^2\cosh^{-1}(N/f)}{N_o^2\cosh^{-1}(N_o/f_o)}\hat{E}^2\frac{3(R_\omega+1)}{4R_\omega}\sqrt{\frac{2}{R_\omega-1}}\ [\mathrm{Wkg}^{-1}]. \tag{40}$$

Expression (40) is obtained by scaling the value of turbulent production for the GM spectrum obtained in section 3.1 (i.e., 8×10^{-10} W kg^{-1}) by two sets of factors. The first is the ratio of $F(m) \propto fN^2\cosh^{-1}(N/f)E_o^2$ (see expression (27)) scaled by GM model parameters; this ratio may be reduced to $\frac{f}{f_o}\frac{N^2\cosh^{-1}(N/f)}{N_o^2\cosh^{-1}(N_o/f_o)}\ \hat{E}^2$. The second set of factors encompasses two frequency-related corrections outlined in section 3.2.1, i.e., the ratio $E(m_c)/E_k(m_c) = (R_\omega+1)/R_\omega$ estimated from observations divided by the same ratio evaluated for the GM model (i.e., 4/3); and an aspect ratio-related correction, $\sqrt{2/(R_\omega-1)}$. Formula (40) is a biased estimate of (18) for non-GM spectra.

Expression (40) has been tested by reference to microstructure observations by both *Polzin et al*. [1995] and *Gregg et al*. [2003], and found to enjoy remarkable agreement with those measurements We focus here on issues of bias as these are most germane to understanding how finescale parameterization estimates relate to large-scale budgets. With regards to random uncertainty in the validation studies, note that the correlation scale of turbulent dissipation is approximately $1/2m_c - 1/m_c$ [*Gregg et al*., 1993]. Vertical shear is sensibly modeled as a Gaussian white process [*Polzin*, 1996], so uncertainty in the production estimates can be obtained assuming shear variance is chi-squared-two with correlation of $1/m_c$ and propagating that uncertainty through the production formulae [*Polzin et al*., 1995]. *Polzin et al*. [1995] and *Gregg et al*. [2003] model validation studies have $O(100)$ degrees of freedom and (crudely) a factor of two uncertainty in both turbulent production and dissipation estimates. Those two studies use slightly different versions of (40), set apart by the application (in Gregg et al.'s case) or not (in Polzin et al.'s case) of the hydrostatic approximation in (30). We note, however, that hydrostatic and nonhydrostatic estimates of the aspect ratio differ by less than 2% for $R_\omega > 1.1$, so that this issue is insignificant for wavefields with near-inertial contributions.

4. Implementation of Finescale Parameterizations

In this section, we discuss how to best implement the finescale parameterization formula (40) in a manner that is most consistent with its underlying physics. Our discussion focusses initially on general issues, and later tackles challenges associated with common instrumentation.

4.1. General Issues

4.1.1. Buoyancy Frequency Algorithms

An aspect of the implementation of finescale parameterizations that has potential to lead to significant errors is the calculation of the buoyancy frequency, $N(z)$, and interpretation of its variability. The buoyancy frequency enters expression (40) both explicitly and implicitly, in the definitions of $\hat{E}^2$ and R_ω. Errors in buoyancy frequency, δN, may be readily shown to propagate as $K_\rho \sim [N/(N\pm\delta N)]^4$, so that a bias in N of a factor of 2–3 implies a bias in the nondimensional energy density $\hat{E}$ of a factor of 4–9, and a bias in K_ρ (or, equivalently, $\mathcal{P}/N^2$) of a factor of 16–81. The occurrence of a bias in N of the stated magnitude may seem large, but is entirely possible (Figure 3).

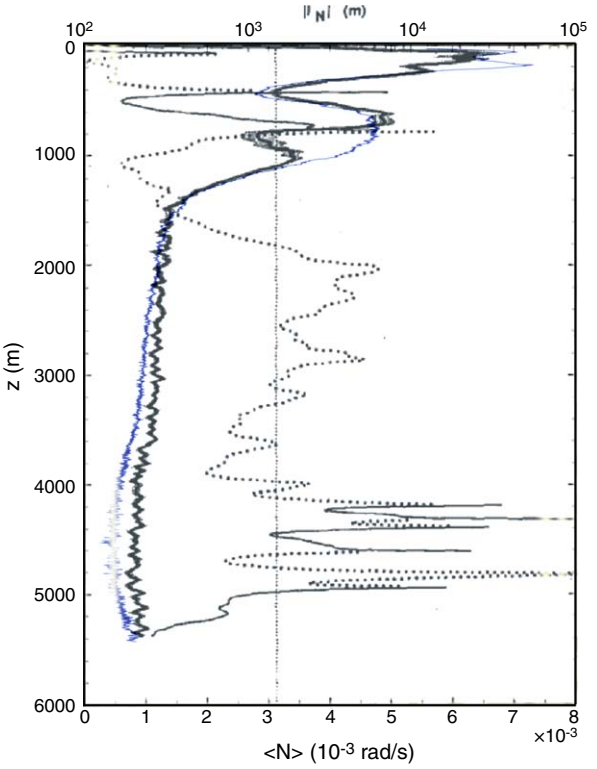

Figure 3. Buoyancy frequency profiles from the Western North Atlantic—MODE. The blue line represents data obtained from hydrographic casts during the mesoscale mapping exercise and is within several hundred kilometers and several months of the MODE-EMVP survey. This curve is overlain upon a figure from *Kunze and Sanford* [1996] representing the mean buoyancy frequency profile from MODE. There are factor of 2–3 differences which translate into factor of 2^4 to 3^4 biases in finescale parameterization estimates for K_ρ.

While seemingly straightforward, attention needs to be paid to algorithms for estimating N^2. We recommend using either the adiabatic leveling method [*Bray and Fofonoff*, 1983], sorting a neutral density profile such that it is statically stable and estimating vertical gradients of the sorted neutral density profile, or the adiabatic correction method with an accurate representation of the speed of sound [*Millard et al*., 1990]. The adiabatic leveling method compares differences in the specific volume anomaly of two parcels displaced adiabatically and isentropically to their average pressure. The neutral density variable [*Jackett and McDougall*, 1997] is closely related to the adiabatic leveling method but can differ significantly at high latitude [*Iudicone et al*., 2008]. The adiabatic correction method estimates the stratification as being proportional to the difference between the in situ density gradient and the inverse speed of sound, squared. The adiabatic correction algorithm is subject to subtractive cancellation at weak stratification and high pressure and thus requires a robust sound speed algorithm. A known defect is that the *Chen and Millero* [1977] sound speed algorithm uses a formulation for the adiabatic lapse rate that is inconsistent with the 1980 equation of state (EOS80) [*Millard et al*., 1990]. The adiabatic correction scheme using *Chen and Millero* [1977] is biased to higher values of N^2, with a typical bias of 10% in N^2 at $N=5\times10^{-4}$ s^{-1}, increasing to higher percentages at lower stratification. We have compared N^2 estimates using both the adiabatic leveling and adiabatic correction methods, and find that the increasingly large shear-to-strain ratios with decreasing stratification at $N < 5\times10^{-4}$ s^{-1} found by *Kunze et al*. [2006] (their Figure 3) are open to interpretation as an artifact resulting from the bias associated with the adiabatic correction method.

4.1.2. Finestructure Contamination

The finescale parameterizations (18) and (19) assume that observations of buoyancy gradients are composed of a time-mean or "background" component, $\overline{N^2}(z)$, and finescale variability associated with the internal wavefield. Strictly, it is $\overline{N^2}$ that must be used in the $N^2\cosh^{-1}(N/f)$ and $\hat{E}^2$ terms in (40), as well as in defining a wave-induced isopycnal displacement η through

$$\begin{aligned}\rho &= \bar{\rho} + \eta\bar{\rho}_z + \frac{1}{2}\eta^2\bar{\rho}_{zz} + \text{higher order terms},\\ \rho_z &= \bar{\rho}_z + \eta_z\bar{\rho}_z + \text{higher order terms},\end{aligned} \tag{41}$$

which enter the definitions of potential energy and strain variance,

$$\begin{aligned}E_p &= \frac{1}{2}\overline{N^2}\eta^2\\ 2m^2E_p = \overline{N^2}\eta_z^2 &= \left[\frac{(N^2(z)-\overline{N^2}(z))}{\overline{N^2}(z)}\right]^2\end{aligned} \tag{42}$$

central to the calculation of R_ω. Ideally, one should define $\overline{N^2}$ on the basis of a time mean, calculated by averaging many measured profiles of N^2 at any one site. However, a single profile is all that is commonly available. In this situation, one has little choice but to assert that a vertical scale separation exists between a large-scale background stratification, dominated by subinertial time scales, and the finescale internal wave signatures. Such a scale separation is implicit in the truncation of the Taylor series expansion in (41). While this assertion is often valid, it breaks down in contexts with significant nonwave contributions to density finestructure.

One of these breakdowns occurs in conjunction with formation of a seasonal thermocline by upper-ocean atmospheric forcing and the subsequent subduction of those waters. A quantitative criterion can be had from a length scale defined from a diapycnal diffusion equation:

$$\frac{\partial \bar{b}}{\partial t} = K_\rho \frac{\partial^2 \bar{b}}{\partial^2 z} \quad .$$

If a water parcel has been away from the boundary for a time τ, the scale h separating wave and mean components should reflect this: $h = \sqrt{K_\rho \tau}$. After 6 months, the vertical wavelength associated with $K_\rho = 1 \times 10^{-5}$ m^2 s^{-1} is $\lambda_v = 2\pi h = 100$ m. This scale is small and thus seasonal thermoclines can be highly problematic regions in obtaining robust estimates of uncontaminated wave displacement and strain from isolated profiles. In *Mauritzen et al*. [2002], the upper 250 m using a strain-based estimate of $\mathcal{P}$ are not shown as they are large and judged to be so contaminated. Similar judgments are offered in *Kunze et al*. [2006].

Finescale buoyancy variability may have a quasi-permanent component associated with either (i) the generation of potential vorticity anomalies at boundaries by topographic torques and the consequent injection of those anomalies into the ocean interior [*Kunze and Sanford*, 1993], (ii) internal wave-driven scarring of the thermocline on vertical scales larger than those of overturning events [*Polzin and Ferrari* [2004, section 5.2], and (iii) up-gradient buoyancy fluxes associated with double diffusive phenomena (section 5.3).

The use of shear-strain ratios as a metric of the variable aspect ratio of the internal wavefield only makes physical sense if shear and strain are estimated over the same bandwidth. While some authors have calculated this ratio by evaluating shear variance and strain variance over different vertical wave number ranges (using the GM model as a common reference), we recommend that a common wave number band is used to avoid biasing the estimation of R_ω for nonwhite (i.e., non-GM-shaped) shear and strain spectra.

4.1.3. Statistical Inhomogeneity and Sampling Bias

The spectral methods underpinning the calculations of many of the variables entering finescale parameterizations assume that the data to which these are applied are spatially homogeneous. This will assuredly not be true if the rate of turbulent dissipation increases dramatically toward the ocean floor as is characteristic of the deep Brazil Basin. While the theory explicitly addresses spatial inhomogeneity with $\mathcal{P}(z) \propto E(m_c, z)^2$, application of the finescale parameterization to the data requires a finite vertical piece length in order to estimate $E(m_c, z)$:

$$E(m,z) \cong \frac{1}{z_2 - z_1} \int_{z_1}^{z_2} E(m,z')dz',$$

from which one estimates $E(m_c, z)$ and then squares the result to estimate $\mathcal{P}(z)$. The windowing procedure implicit in a Fourier transform technique further obscures the nature of the relationship between average spectral level and turbulent production. Using the analytic solutions for $E(m,z)$ and $\mathcal{P}(z)$, we estimate a possible bias (underestimate of $\mathcal{P}$ by the finescale parameterization) of a factor of 2 for the Brazil Basin data in *Polzin* [2009].

A second tier of potential biases arise when finescale parameterization estimates are compared with control volume or inverse estimates of diapycnal transfers across an isopycnal surface. Turbulent dissipation tends to be enhanced above rough and steep topography and that connection needs to be adequately represented as one attempts to extrapolate sparse finestructure information over the spatial extent of the large-scale budget. In the Brazil Basin TRE data sets, High Resolution Profiler sampling was concentrated in relatively flat and well sedimented fracture zone valleys, biasing the data away from the issue of mixing above

rough topography [*Polzin*, 2009]. Similar choices could be a common affliction for hydrographic stations [*Thurnherr and Speer*, 2003]. Temporal biasing not need be so obvious. For example, in MODE and PolyMode, AVP and EMVP profiles were obtained over both topologically smooth and rough regions, but sampling over rough topography excluded times when low frequency near bottom currents were equal to or greater than their climatological values. This would tend to diminish an internal lee wave generation signature and *Kunze and Sanford* [1996]'s conclusion that the region only supports background mixing could be substantially impacted. In a similar vein, hydrographic lines may transect hot spots for internal tide generation and mixing, but those hot spots could be sampled during neap tide conditions. The assessment of control volume budgets relative to finescale and microscale mixing estimates is likely to be an iterative process.

4.2. Instrumentation-Related Issues

As noted above, the estimation of the various terms in the finescale parameterization (40) relies on observations of density and velocity finestructure. In the following, we discuss the limitations of common instrumentation in resolving finescale internal wave signals, and advise on how to deal with these shortcomings.

4.2.1. CTD Density Data

The main limitation of CTD measurements obtained in standard hydrographic surveys is related to the variability in the CTD package's fall rate, w. There are two ways in which this variability can result in contamination of the density finestructure measurements. The first stems from a characteristic mismatch between the response times of conductivity and temperature sensors [*Horne and Toole*, 1980], combined with a mismatch in the scaling of each sensor's response time with the package's fall rate [*Schmitt et al*., 2005a]. For example, a freely flushing conductivity cell's response time is simply the time that it takes to replace water in the cell and is inversely proportional to the fall rate. In contrast, the response time of a small thermometer is limited by the diffusion of thermal anomalies through the viscous boundary layer and the material of the sensing element [*Lueck et al*., 1977]. The boundary layer height (and hence the thermometer's response time) is dependent on the fall rate, potentially scaling as $w^{1/3}$ [*Lueck et al*., 1977]. Complications also arise with the thermal inertia of a conductivity cell heating water during the sampling process [*Lueck*, 1990; *Lueck and Picklo*, 1990].

The second way in which variability in w leads to contamination of CTD finestructure measurements involves the entrainment of water within the rosette frame as a result of the package's inertia [*Toole et al*., 1997]. The entrained water may overshoot the CTD sensors as the package decelerates, leading to the same water being sampled twice.

Irrespective of the dominant source of CTD finestructure contamination, ship heave in surface swell can be shown to be transmitted to the CTD package. Since the package is typically lowered at rates of $\sim$1 m s^{-1} and swell is characterized by a period of $\sim$10 s, variations in the package descent rate map onto contamination at vertical wavelengths of $\sim$10 m. This contamination can be diagnosed by creating a time series of the fall rate from the CTD pressure record, and comparing the spectra of that time series with the CTD density spectrum. Density finestructure contamination shows up as a peak centered at the wave number of maximum fall rate variability (Figure 4).

4.2.2. Velocity Data

Internal wave shear may be plausibly characterized as Gaussian with a white spectrum [*Polzin*, 1996]. Thus, the presence of instrumental noise in measured velocity or shear profiles is difficult to ascertain, and a quantification of noise is commonly clearest in the spectral domain. Below, we outline the noise characteristics of two measuring systems that are regularly used to acquire velocity finestructure data: lowered Acoustic Doppler Current Profilers (LADCPs) and electromagnetic (EM) velocity sensors.

4.2.2.1. Lowered Acoustic Doppler Current Profilers

The operating principle of a Doppler sonar is to transmit an acoustic pulse and determine the Doppler shift of the backscattered signal. These Doppler shifts are interpreted as slant velocities of suspended acoustic backscattering targets moving with the water relative to the instrument platform and information from multiple beams is used to obtain estimates of the oceanic horizontal velocity field. Doppler sonar systems have intrinsic limitations in their ability to determine the phase shift of a backscattered acoustic signal (see *RDInstruments* [1996] for a succinct description of the theoretical principles and *Theriault* [1986] for an in-depth assessment). These limitations are predicted to result in ping-to-ping uncorrelated noise with a theoretical single-ping accuracy of ϑ ($=$ 3.2 cm s^{-1} in the application discussed here), decreased by a factor of $\sqrt{n}$ after

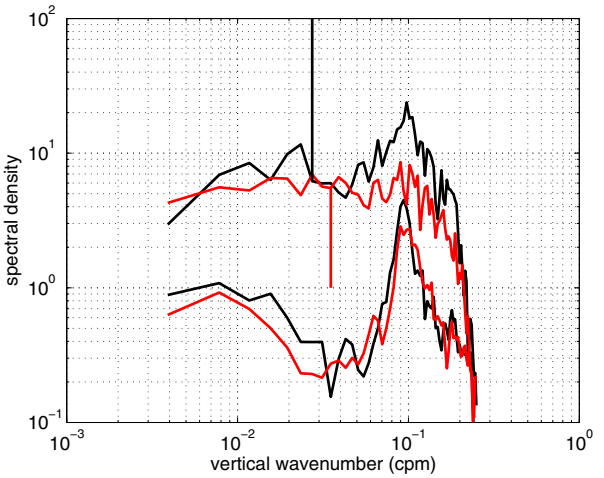

Figure 4. CTD density profiles from I8S. Red = 539–793 db, black = 939–1193 db. Upper traces are strain spectra, lower traces are fall rate variability spectra. The vertical lines depict the cutoff wave number based upon the criterion that $\int_0^{m_c} 2m^2 E_p dm = 2\pi N^2/30$. The strain spectra at higher wave numbers are noisy and do not roll-off like those from free-fall instrumentation. The implication is that CTD data obtained with wire-lowered systems are contaminated by heaving of the package in response to surface swell. The degree of contamination will depend upon sea state, lowering rate, sensors (here a Neil Brown Instrument Systems CTD was used), variability of the $\theta - S$ relation and configuration of the sensors and Nisken bottles about the Rosette package.

averaging n pings in a single depth bin (typically 45 pings are averaged per bin in the 5 m binned data examined here) and having a bandwidth (BW) equal to the Nyquist wave number of the averaging interval (e.g., a BW of 0.1 cpm for 5 m binned data). The University of Hawai'i data acquisition algorithm [*Fischer and Visbeck*, 1993] acts on the raw data by first differencing to obtain an estimate of vertical shear and then interpolating those shear estimates onto a uniform depth grid. These operations result in an attenuation of both noise and signal by factors of $\mathrm{sinc}^2(m\Delta_r)$ (where Δ_r is the finite range gate of the received signal), and $\mathrm{sinc}^4(m\Delta_r)\mathrm{sinc}^2(m\Delta_g)$, respectively, in which the depth grid has spacing Δ_g [*Polzin et al.*, 2002]. The implied energy spectrum of the LADCP noise is

$$E_n(m) = \frac{1}{2}\frac{2\vartheta^2 \mathrm{sinc}^6(m\Delta_r)\mathrm{sinc}^2(m\Delta_g)}{n \times BW}. \quad (43)$$

Further attenuation of the noise may be expected from LADCP beam separation effects and tilting of the CTD/LADCP package. While the noise model (43) provides a reasonable scaling of the observed noise, measured rms noise levels tend to be larger than this theoretical limit (43) by a factor of 2–4 [*Plueddemann*, 1992], and care is required to avoid interpreting this noise as a signal. Note also that this noise model applies to data processed with the University of Hawai'i LADCP data acquisition software. The standard output of that algorithm *decimates* the 5 m data onto a 20 m grid rather than *average* the 5 m data over 20 m bins. The choice of decimation rather than averaging results in a fourfold increase in the noise spectrum and factor of two decrease in usable bandwidth. An alternative common processing algorithm [*Visbeck*, 2002] affects substantially less smoothing on the data, but its attenuation properties have not yet been quantified.

In the absence of a precise metric of LADCP noise as a function of wave number, we advise that examination of the polarization characteristics of LADCP shear may usefully inform the parameterization user's choice of the highest vertical wave number that may be considered resolved by the available observations. An illustration of this point is provided by data from the southern Drake Passage in Figure 5. Here we find a consistent signature of clockwise phase rotation with depth dominating counter-clockwise, and shear-to-strain ratios of $O(10)$ at vertical wavelengths in excess of 80 m. The observed spectra are well in excess of the noise model (43). If these ancillary information (noise and polarization characteristics) are not revealing, we recommend that the choice of the upper vertical wave number limit is made conservatively.

4.2.2.2. Electromagnetic (EM) Velocity Sensors

The use of EM velocity sensors mounted on vertical profilers to sense motionally induced electric and magnetic fields [*Sanford*, 1971] in the ocean provides velocity data that is better conditioned to the application of finestructure parameterizations than that acquired by Doppler sonar systems. The technique has seen greater application in process-oriented studies than in hydrographic sections, for which LADCP usage has become common in recent years. The principal limitation of EM velocity data is the measurement error induced by vibration, electronic, and electrode noise [*Sanford et al.*, 1982]. The rotation rate of the EM sensor platform and the separation between electrode pairs are important variables in determining the instrument's signal-to-noise ratio.

The physical principle of the measurement is to estimate the voltage drop associated with the motion of a conductor (sea water) in the Earth's magnetic field. In order to eliminate biases in the system, the leads of the

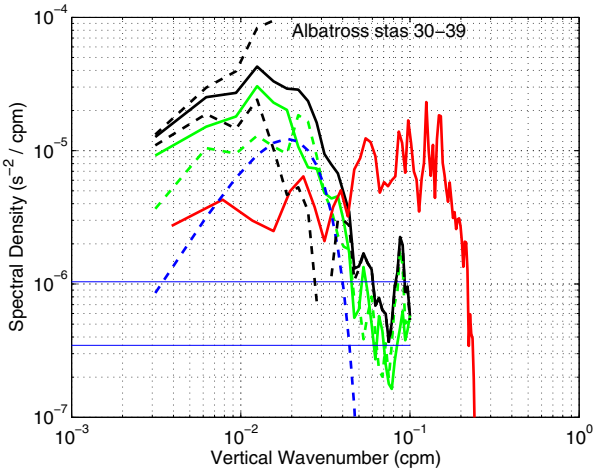

Figure 5. Lowered ADCP velocity and CTD density profiles from the southern Scotia Sea—Albatross stations 30–39 at depths of 3210–3525 m. The mean stratification is $\overline{N^2} = 1.65 \times 10^{-7}$ s^{-2}. Color and line coding: green solid = $2m^2E_{cw}$, green dashed = $2m^2E_{ccw}$, black solid = $2m^2E_k$, red = $2m^2E_p$, blue dashed = $10E_n$ and two black dashed traces, $2m^2E_{cw} + 2m^2E_{ccw}$ and $2m^2(E_{cw} + E_{ccw} - 10E_n)$ that have been corrected for smoothing. The thin horizontal lines represent the high wave number asymptotes of twice the GM E_k and E_p gradient spectra. The shear spectrum is fully resolved at a vertical wavelength larger than 100 m; noise and or smoothing modify the estimate of E^2 [i.e., $(20)^{-2}$] by less than a factor of two. *Garabato et al.* [2004a] interpret this enhanced finestructure as supporting significantly enhanced abyssal mixing. *Kunze et al.* [2006] regard the enhanced finestructure as an artifact of instrument noise in a weakly stratified environment. We conclude that concerns expressed in *Kunze et al.* [2006] regarding the contribution of noise to large finescale parameterization estimates of abyssal mixing attributed to the Albatross data set in *Garabato et al.* [2004a] are not supported by the data.

voltmeter are effectively switched by rotating the instrument and then fitting sinusoids at the period of rotation to a data segment of length Δ_{fit} to the resulting output. A working model is to assume white noise of amplitude ϑ in each geographic coordinate, with a bandwidth given by the Nyquist wave number of the processed profiles. For the EM Velocity Profiler (EMVP), $\vartheta = 0.5$ cm s^{-1}. Expendable Current Profilers (XCPs) have higher noise levels (a nominal $\vartheta = 0.7$ cm s^{-1}) [*Sanford et al.*, 1982, 1993]. The resulting noise in the energy spectrum is given by

$$E_n = \frac{1}{2} 2\vartheta^2 \mathrm{sinc}^2(m\Delta_{fit}) / BW. \quad (44)$$

Given two electrode pairs on a single instrument, the amplitude of the noise can be determined by differencing the two independent velocity estimates. The noise model (44) was validated using Monte-Carlo simulations to ascertain that the process of fitting sinusoids would result in the attenuation described by the sinc-function, Figure 6.

EMVP data from the Mid-Ocean Dynamics Experiment (MODE) have received attention in a number of contexts [*Sanford*, 1975; *Garrett and Munk*, 1975; *Leaman and Sanford*, 1975; *Leaman*, 1976; *Kunze and Sanford*, 1996; *Polzin*, 2008]. As a historical note, estimates of the high wave number roll-off of MODE data figure prominently [*Polzin and Lvov*, 2011] in *Garrett and Munk* [1975]'s adoption of $m^{-2.5}$ as representing the background internal wavefield. Here we find that noise and smoothing serendipitously offset so that estimates of dissipation via the finescale parameterization are within a factor of two of results published in *Kunze and Sanford* [1996], buoyancy frequency-related issues (Figure 3) aside.

4.2.2.3. Moored Profiler

The Moored Profiler [*Doherty et al.*, 1999] utilizes a motorized traction drive to crawl up and down a mooring cable. The platform is instrumented with both an acoustic travel time velocity sensor to estimate relative flow past the profiler and a CTD. *Doherty et al.* [1999] find velocity noise to be primarily associated with platform vibrations while profiling along the irregular mooring wire. They quote standard errors in 2 m averaged velocity estimates of $\vartheta \leq 0.6$ cm/s. Assuming a white noise spectral representation provides

$$E_n = \frac{1}{2} 2\vartheta^2 / BW. \quad (45)$$

4.3. Summary

To conclude this section, we regard an understanding of the instrumental response (smoothing and noise characteristics) as being an essential part of interpreting data via finescale parameterizations. If smoothing effects dominate noise, some correction can be justified, but only with extreme caution.

5. Application of Finescale Parameterizations

The conceptual map of dynamical processes in the vertical wave number—frequency domain shown in Figure 1 is expressed in observations in the manner illustrated by Figure 7. At vertical wave numbers smaller

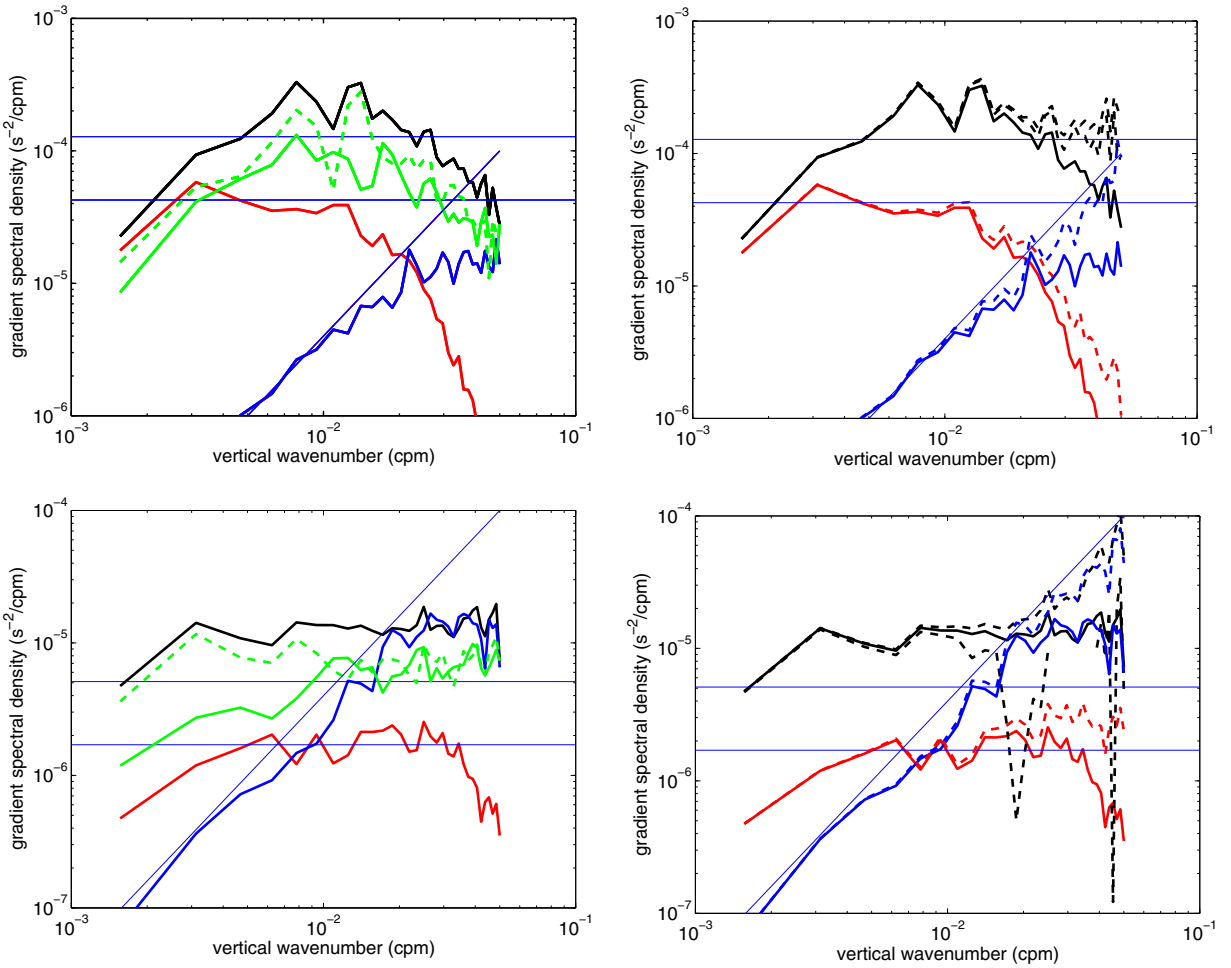

Figure 6. EMVP data from MODE. (top) Thermocline (540–850 m, $\overline{N^2} = 1.8\times10^{-5}$ s^{-2}); (bottom) Abyssal (3040–3350 m, $\overline{N^2} = 7.3\times10^{-7}$ s^{-2}); The left-hand plots display the observed spectra: black $= 2m^2E_k$, green $= 2m^2E_{cw}$ (solid), and $2m^2E_{ccw}$ (dashed), red $= 2m^2E_p$ and blue $= 2m^2E_n$. The noise spectrum is taken as the difference of the two independent estimates of velocity from the EM sensor. The thin blue line represents a white velocity noise spectrum. The right-hand plots display the observed shear (black) noise (blue) and strain (red) spectra as solid lines. Dashed lines represent attempts to subtract the noise contribution from the shear spectra and then correct both shear and strain spectra for smoothing. The thin horizontal lines represent the high wave number asymptotes of twice the GM E_k and E_p gradient spectra.

than 0.1 cpm, the shear spectrum is relatively white. Turbulence appears as a hump at much higher wave number, greater than 1 cpm. In between, there is a transition regime where the shear spectrum approximately displays an $m^2E_k(m)/N^2 \propto m^{-1}$ dependence. This transition regime is characterized by strongly nonlinear dynamics and spectrally nonlocal transports of energy associated with shear instability (8). A finescale parameterization seeks to predict the high-wave number hump from the characteristics of the shear spectrum at wave numbers smaller than those of the transition region, as the integral (in the vertical wave number domain) of the high-wave number hump is proportional to the turbulent dissipation rate.

In this section, we illustrate the successes and failures of finescale parameterizations by reviewing a range of published applications to specific oceanic data sets. We commence with a data set for which parameterization application is straightforward and successful, and then explore other data sets to demonstrate possible pitfalls with making assumptions that deviate from the parameterization recipe.

5.1. Far Field of the Abrupt Topography Experiment

We start by examining a set of measurements that were obtained as part of the Abrupt Topography Experiment [e.g., *Brink*, 1995; *Eriksen*, 1998]. The goal of the Abrupt Topography Experiment was to study the dynamics of a vortex capping the seamount and internal waves on the steeply sloping sides. We use data obtained in the far field of Fieberling Guyot as an illustration of a context in which the physical assumptions

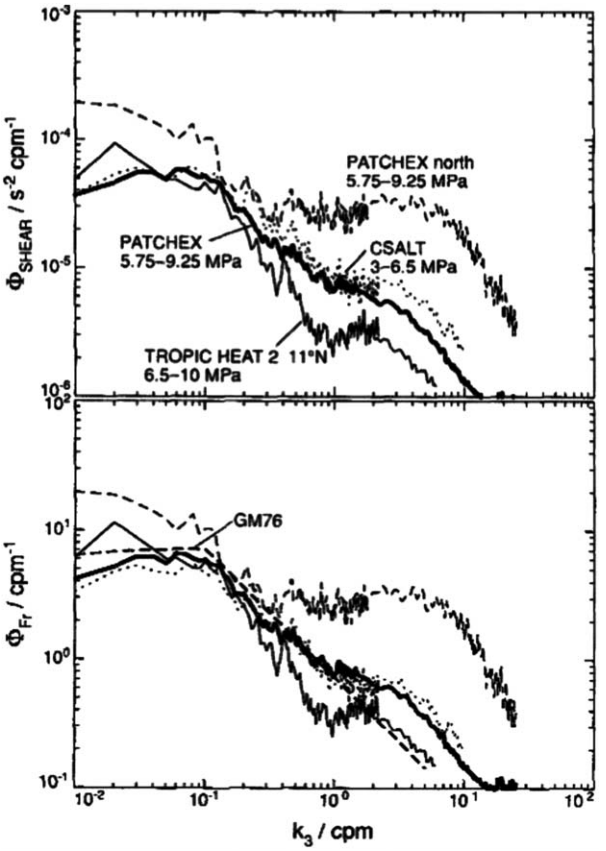

Figure 7. Composite shear spectra from *Gregg et al.* [1993]. Low wave number ($m < 2$ cpm) spectra were obtained with an acoustic travel time current meter. High wave number ($m > 1$ cpm) spectra were obtained with airfoil shear probes. The finescale parameterization is an attempt to relate the spectra at low wave number ($m < m_c$) to the integral of the shear spectrum at wave numbers greater than the Ozmidov length, $m > (2\pi L_o)^{-1}$, expressed as the rate of dissipation of turbulent kinetic energy, $\epsilon = \frac{15}{4}\nu\int_{1/2\pi L_o}^{\infty} 2m^2 E_k(m)dm$, skipping the intermediate range of wave numbers $m_c < m < (2\pi L_o)^{-1}$. See the schematic in Figure 1.

of the finescale parameterizations hold, resulting in successful predictions of the turbulent dissipation rate. In this and subsequent examples, we first review observations of the shear and strain spectra that are input to the parameterizations and (using expression (20)) determine the wave number m_c at which a transition to wave-breaking phenomena occurs. Then, we calculate the rate of spectral energy transport through the vertical wave number domain, $F(m)$, using both (18) and (19). Finally, we compare the outcomes of this calculation to the spectral energy transport predicted by a model of shear instability in the wave-breaking region of the vertical wave number domain (8) and to a microstructure-derived estimate of the rate of turbulent production $\mathcal{P}$ (4). By comparing the estimates of $F(m)$ with the "measurement" of $\mathcal{P}$, we are able to assess the performance of the finescale parameterization.

5.1.1. Shear and Strain Spectra

Buoyancy-scaled spectra of shear and strain (Figure 8) can be distinguished from the GM model in two aspects. First, they are somewhat whiter, with an $m^{-1.8}$ power law (c.f. an m^{-2} power law in the GM model). Second, the transition to the wave-breaking regime with m^{-3} power law occurs at a smaller wave number in observations ($m_c < 0.1$ cpm) than in the GM model. Nonbuoyancy scaled shear spectra (Figure 9) can similarly be contrasted with the canonical shear spectrum described by *Gargett et al.* [1981]: they are white at wave numbers lower than m_c and roll-off as approximately m^{-1} at higher wave numbers. Shear spectra from many sites in the ocean tend to do this (Figure 7), but there are some notable exceptions, e.g. *Duda and Cox* [1989].

The picture is less clear when one examines strain spectra (Figure 8). The naïve expectation would be that the strain spectrum mimics the variability in the canonical shear spectrum. Aside of any discussion about power laws or definitions of the cutoff wave number m_c, there is a trend of decreasing kinetic to potential energy ratios with increasing vertical wave number, *Polzin et al.* [2003]. Linear internal wave kinematics would imply an increasing contribution of high-frequency waves, but this does not appear to be the case. Rather, it has been interpreted as a signature of an increasing contamination of the finescale field by quasi-permanent finestructure [*Polzin et al.*, 2003] likely associated with rotating stratified turbulence [*Polzin and Ferrari*, 2004]. A corresponding representation in the horizontal wave number domain and interpretation as stratified turbulence is given in *Klymak and Moum* [2007a, b]. The decrease in shear-to-strain ratio with increasing vertical wave number is noticeable, but not large, at and prior to m_c in this example (Figure 8).

Interpretation of the observed finescale shear-to-strain ratios as resulting from a wavefield having an aspect ratio independent of vertical wave number contaminated by a quasi-permanent finestructure field is abetted by our dynamical ignorance regarding nonlinear energy transports in the frequency domain [*Polzin and Lvov*, 2011]. Only one definite assertion can be made: the resonant summary provided by *McComas and Müller* [1981] features a transport of energy to *lower* frequency which would imply *increasing* shear-strain

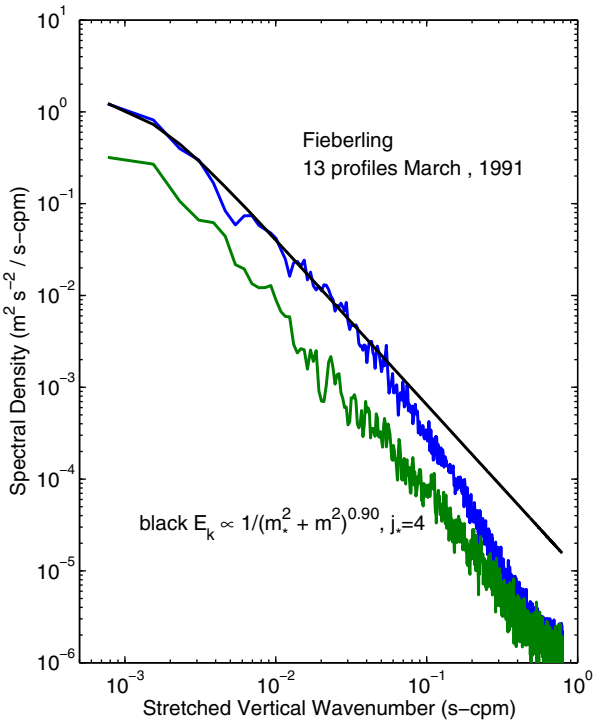

Figure 8. Kinetic (blue) and potential (green) energy spectra from the far field of Fieberling Guyot during the Abrupt Topography experiment. Data have been buoyancy scaled in amplitude and vertical coordinate prior to the spectral analysis. The black curve represents a fit of $E_k = 1/(m_*^2+m^2)^{0.9}$, with m_* equal to the equivalent of mode-4 ($j_*=4$), following the analysis in *Polzin and Lvov* [2011].

ratios with *increasing* vertical wave number. That resonant summary is understood to be internally inconsistent, incomplete and requires a source of wave energy at high frequency that has not been observed [*Polzin and Lvov*, 2011]. Examples of finescale spectra with increasing quasi-permanent (nonwave) finestructure contamination are given in the following two subsections.

Observational tests to date [*Polzin et al*., 2003] have characterized ϕ as being independent of vertical wave number, and thus have not dealt with the issue of nonseparable frequency-vertical wave number spectra. We recommend taking a representative value of R_ω at intermediate vertical scales if contamination is believed to be an issue.

5.1.2. Estimates of Spectral Energy Transports

Calculating the rate of spectral energy transport through the vertical wave number domain, $F(m)$, using both (18) and (19), yields estimates that increase with increasing vertical wave number, hit a plateau at wave numbers $m \leq m_c$, and decrease thereafter. Decreasing shear-to-strain ratios help maintain a relatively broad plateau in the vicinity of m_c. Nonlinear transport estimates decrease at higher wave number in association with increasing shear instability transports (8), clearly delineating the limit of applicability of the finescale parameterizations in the vertical wave number domain. The strain spectrum has been assumed to represent internal wave variability in this calculation.

A robust prediction of spectral energy transport can be obtained, in this case study, for wave numbers $m_c/5 < m \leq m_c$. At both lower and higher wave numbers, the transport estimates are smaller than the microstructure-derived turbulent production rate. The disparity between $\mathcal{P}$ and $F(m_c)$ (40) ranges from a factor of 0.7 to a factor of 1.5.

5.2. The North Atlantic Tracer Release Experiment

5.2.1. Shear and Strain Spectra

Finestructure shear and strain spectra from NATRE exhibit a steep (red) vertical wave number dependence and have a large bandwidth, Figure 10. There is an obvious decrease of shear-to-strain ratio with increasing vertical wave number that has been quantitatively interpreted using a model of linear internal waves refracting from a quasi-permanent density finestructure field [*Polzin et al*., 2003; *Polzin and Ferrari*, 2004]. That model predicts quasi-permanent finestructure shear and strain spectra that peak at vertical wavelengths slightly larger than $1/m_c$. The residual (observed minus quasi-permanent) has shear-to-strain ratios (and hence aspect ratios) that are nearly independent of vertical wave number and lends credence to the notion [*Polzin*, 2004a] of energy transports in the frequency domain, G, being small. However, caution with applying finescale parameterizations is required as the near-inertial field appears to be set up in response to forcing from the baroclinic tide via a parametric subharmonic instability (K. L. Polzin, A regional characterization of the Eastern Subtropical Atlantic internal wave spectrum, manuscript in preparation, 2011).

5.2.2. Estimates of Spectral Energy Transports

Shear spectra observed during NATRE roll-off quite steeply, and thus spectral energy transport estimates do not converge, Figure 11. Agreement of $\mathcal{P}=(1+R_f)\epsilon$ with $F(m)$ ((18) and (19)) is obtained at high wave

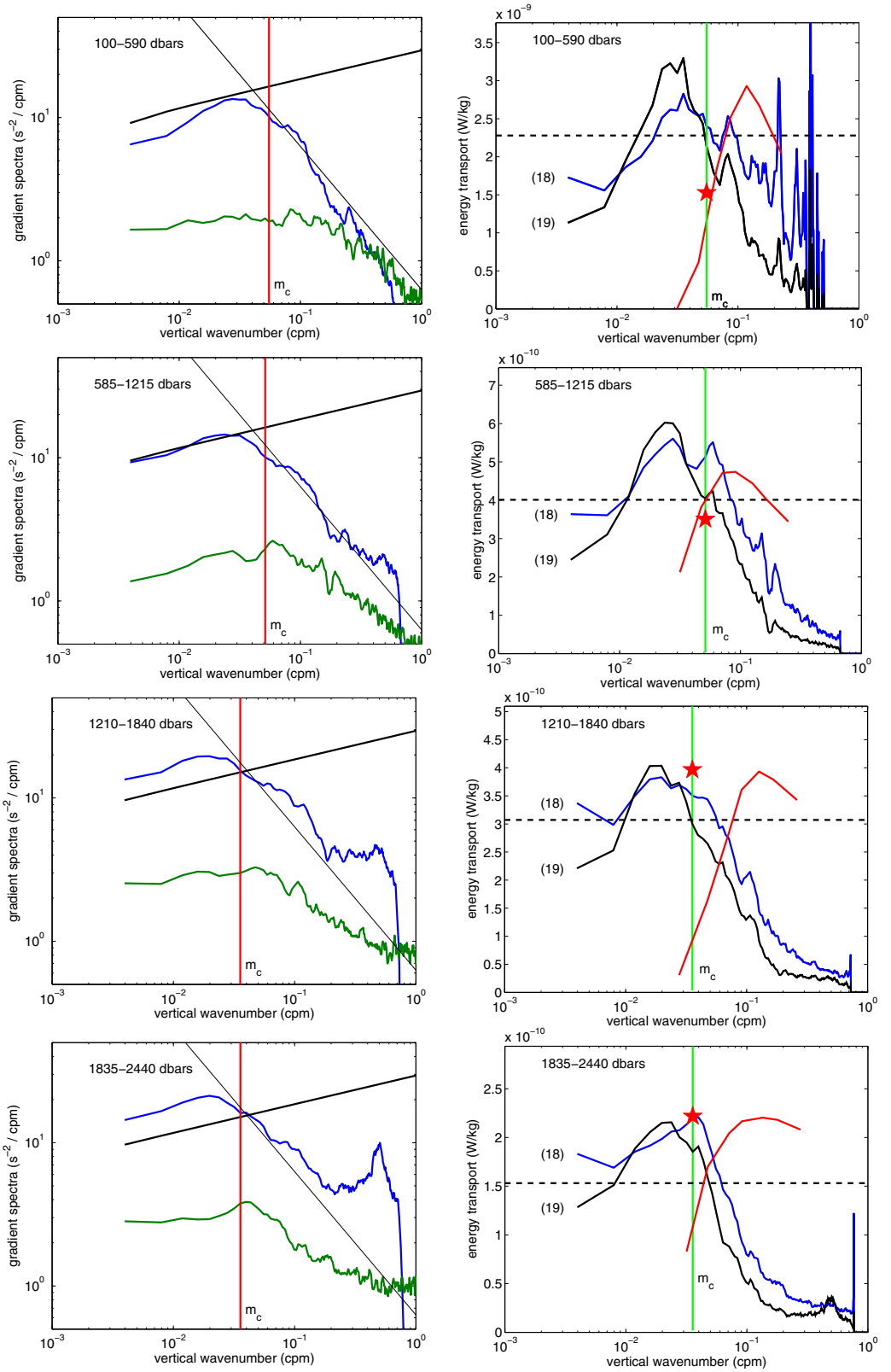

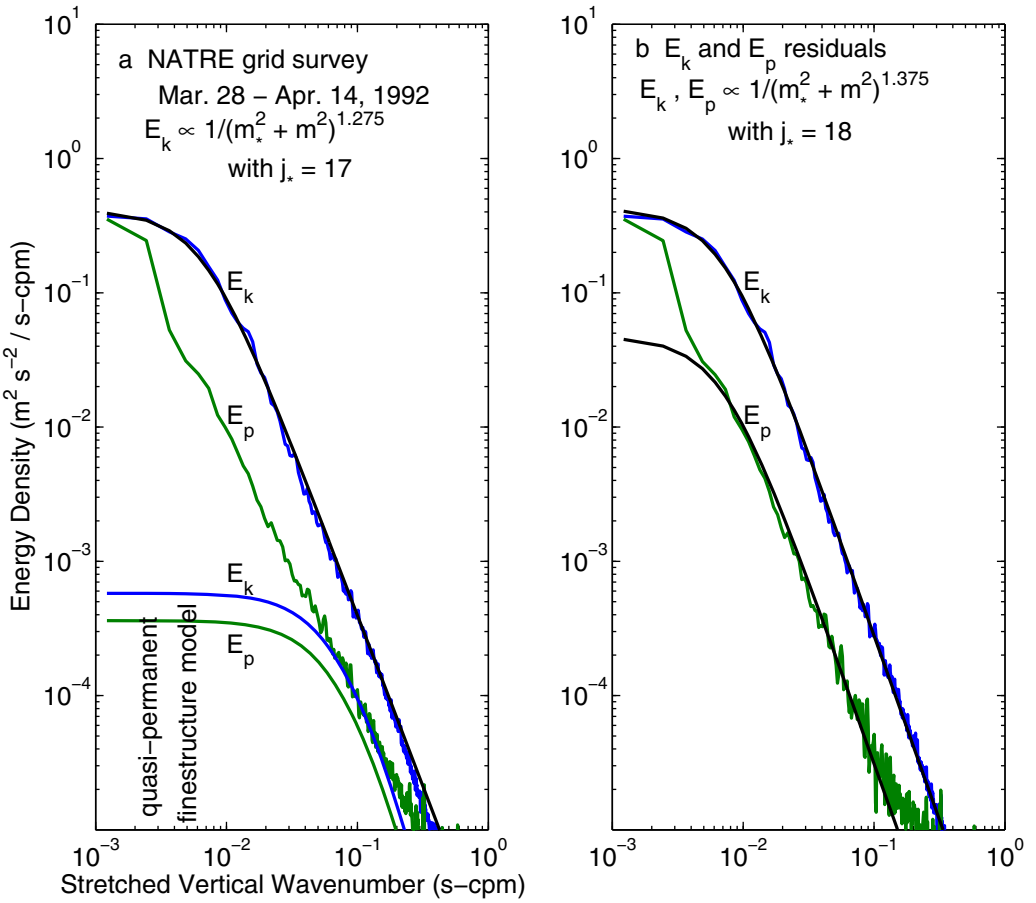

Figure 10. Natre vertical wave number kinetic E_k and potential E_p energy spectra, figure from *Polzin and Lvov* [2011]. These 100 profiles were obtained as part of a 400 km × 400 km grid survey. (a) Observed vertical spectra, *N*-scaled and stretched under the WKB approximation to $N_o = 3$ cph, and the quasi-permanent finestructure spectrum from *Polzin et al*. [2003]. (b) The internal wave spectra, observed minus quasi-permanent contributions. Black lines represent fits of $1/(m_*^2+m^2)^{11/8}$ to the spectra, with $m_* = 0.0070$ cpm. The fit to the velocity data is obscured as it overlies the data. Note that the low-wave number spectral estimates have typically smaller ratios of E_k and E_p.

number. The disparity between $\mathcal{P}$ and $F(m_c)$, (40) is a factor of 1.4–1.7. If this wavefield were to be sampled with instrumentation having coarser vertical resolution, the potential bias associated with that lack of resolution (section 3.2.2) would be significant (larger than a factor of 2).

K. L. Polzin (manuscript in preparation, 2011) interpret the high bandwidth (large m_*) and peculiarly steep (red) roll-off of the NATRE shear spectra as being associated with the forcing of the near-inertial field by a semidiurnal tide via the PSI (K. L. Polzin, manuscript in preparation, 2011). The inertial field gains energy from the tide at low vertical wave number, but the inertial field is saturated at high wave number and so loses energy to the tide. This saturation process is, essentially, a scale-selection mechanism that determines both the bandwidth and roll-off of the near-inertial wavefield.

Given this departure from the GM spectrum and combination of finescale transports and PSI forcing, we thus anticipate that coarse-resolution estimates of PSI-driven wavefields will typically return a biased

Figure 9. (left) Shear (blue) and strain (green) spectra as a function of depth. The red vertical line in the spectral plots represents the cutoff wave number m_c (20). The thick black curve is the fit to the WKB scaled spectrum in Figure 8. The thin black line represents the "saturated" spectrum, $2m^2E_k(m) = 2\pi N^2 m_c/m$. Spectral estimates used a multitaper method and have been averaged over 3–4 overlapping depth bins. The strain spectra were estimated from neutral density profiles that were sorted to be statically stable. The averaging and windowing procedures are intended to increase statistical reliability and the sorting procedure significantly decreases the high wave number strain variability at low stratification. (right) Transport estimates as a function of depth. The blue and black traces represent the transport estimates (18) and (19). The red star represents the $1+R_f$ times the observed dissipation rate and is plotted at m_c. The black dashed horizontal line represents the transport estimate employed by *Polzin et al*. [1995]. The red curve is the shear-instability transport function (8). The shear instability transport estimates are regarded only as being qualitatively robust due to the density sorting procedure. See *Polzin* [1996] for quantitatively robust applications without the sorting procedure.

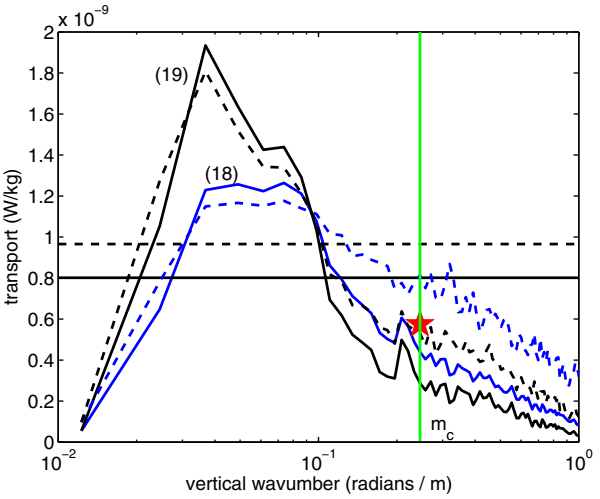

Figure 11. Transport estimates for Natre using (18)—blue and (19)—black. Dashed traces use the observed spectra, solid traces assume a shear-strain ratio of $R_\omega = 9$ attained at low wave number. The cutoff m_c is represented as the green vertical line and $(1+R_f)$ times the observed dissipation is represented as the red symbol. The horizontal lines use spectral levels averaged to m_c to estimate E and R_ω. Note that finescale parameterizations do not converge to a unique estimate of turbulent production, but are quite close to the observed production rate at m_c. Profiles 3–102 from Natre, $\epsilon = 4.9\times10^{-10}$ W/kg and $300 < p < 812$ db.

estimate of the turbulent dissipation rate, and suggest that this may impact the interpretation of *Alford et al*. [2007], who apply a finescale parameterization to shipboard sonar velocity measurements at wavelengths greater than 60 m.

5.3. The Salt Finger Tracer Release Experiment

5.3.1. Shear and Strain Spectra

Shear spectra from the Salt Finger Tracer Release Experiment (SFTRE) are intermediate in character to the previous two examples, with spectral slopes steeper than those from Fieberling Guyot (section 5.5.1) but less steep than those from NATRE (section 5.5.2), and with bandwidths less than those from NATRE but greater than those from Fieberling Guyot (Figure 12). The strain spectra, though, are anomalous even in comparison to the gamut of variability described in *Polzin et al*. [2003]. The anomalous strain spectra likely result from staircase features (Figure 13) that arise from up-gradient buoyancy fluxes associated with double diffusion [*Schmitt*, 1994]. SFTRE represents a case of severe quasi-permanent density finestructure contamination.

5.3.2. Estimates of Spectral Energy Transports

The finescale parameterization spectral energy transport estimates of $\mathcal{P}$ simply do not agree with microstructure-derived turbulent production estimate, Figure 14, *unless* one were to interpret the strain field as being associated with the internal wavefield. We perceive that this is unlikely to be the case based upon measurements of the dispersion of an anthropogenic tracer as part of the experiment [*Schmitt et al*., 2005b].

Gregg et al. [2003] include data from a nearby region also supporting staircase features. We note that their finescale parameterization estimates, as those examined here, exhibit a tendency to underpredict the observed dissipation. We conjecture that there may be a significant contribution of double diffusive convection to the observed dissipation.

5.4. The Southern Ocean Finestructure Project (SOFine)

5.4.1. Shear and Strain Spectra

The Southern Ocean Finestructure (SOFine) project is a British-Australian funded endeavor to understand the role of finestructure and microstructure in relation to the momentum balance of the Antarctic Circumpolar Current (ACC). A single hydrographic survey with lowered ADCP, CTD, and Vertical Microstructure Profiler (VMP) measurements was conducted on the northern flank of the Kergulean Plateau [*Waterman et al*., 2013], a significant obstacle in the path of the ACC that figures prominently in providing the net form drag that balances zonal wind stress in numerical models of the ACC [*Stevens and Ivchenko*, 1997]. Here we extract data from nine stations that are characterized by both $F_r \gtrsim O(0.1)$ and a tendency of the finescale parameterization to overpredict the observed dissipation. Six of the nine profile segments contain data from within 20 m of the bottom. With transform lengths of 640 m and $1/m_c \cong 120$ m, however, the data extend well beyond the near-boundary regime discussed directly below. Rather, we anticipate an issue of wave-mean interactions dominating wave-wave interactions from the time scale ratio (22).

The spectra are well resolved with $1/m_c$ much larger than vertical wavelengths dominated by either noise or instrument response, Figure 15. Low shear-strain ratios at low wave number indicate either a contribution of high frequency waves or quasi-permanent finestructure. However, they do not impact the finescale parameterization's estimate of dissipation via (18) or (19).

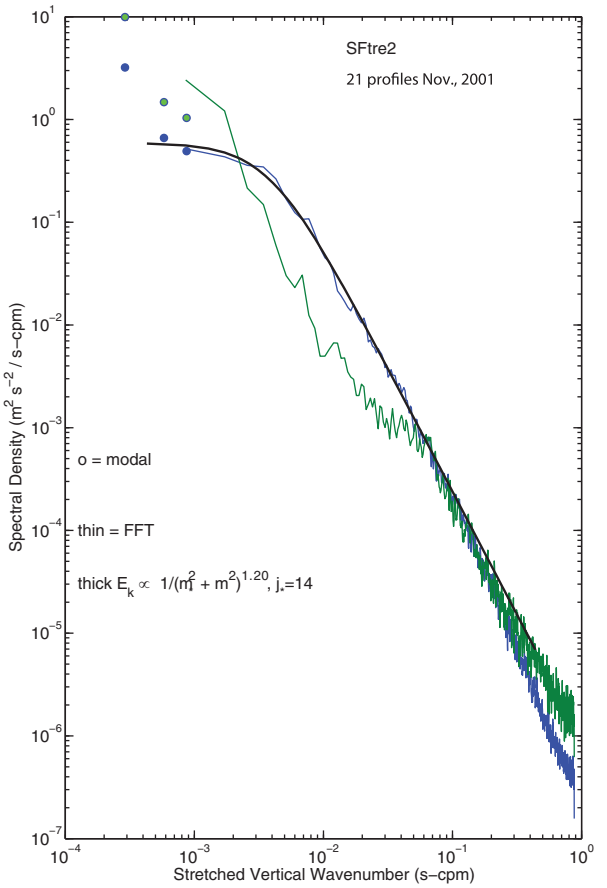

Figure 12. SFtre2 kinetic (blue) and potential (green) energy spectra from *Polzin and Lvov* [2011]. The black curve represents a fit of $E_k = 1/(m_*^2 + m^2)^{1.2}$, with m_* equal to the equivalent of mode-14 ($j_* = 14$). The high wave number E_p spectrum is obviously contaminated by permanent density finestructure (*aka* the staircases) in Figure 13.

5.4.2. Estimates of Spectral Energy Transports

Estimates of dissipation via average spectral levels (32) exceed the observed dissipation rate of 3×10^{-9} W/kg by a factor of 4, and estimates by the eikonal relation (18) or local formulation (19) exceed the average estimates by another factor of two, Fig. 16. The transport estimates are considered to be well resolved and thus the discrepancy between observed dissipation and finestructure dissipation is assumed to represent deterministic wave-mean transports dominating the stochastic wave-wave transports. See *Waterman et al*. [2014] for further discussion of the dynamical interpretation.

5.5. Boundary Conditions and Supercritical Topography

As discussed in section 2, we expect that boundary conditions can short circuit the transport process upon which the finescale parameterization is predicated. Three tests of the finescale parameterization have been made adjacent to topography that is supercritical with respect to the semidiurnal internal tide.

The first example can be found in literature associated with the Hawai'i Ocean Mixing Experiment (HOME). In this context, *Klymak et al*. [2008] apply

$$\epsilon = 1.2\times10^{-9}\frac{<S^2>^2}{<N^2>N_o^2}[\mathrm{W\ kg^{-1}}], \tag{46}$$

with $<S^2>$ estimated as a 4 m first difference to Doppler sonar and CTD data obtained from the Floating Instrument Platform (FLIP). They find agreement between (46) and several different diagnostic estimates of the turbulent dissipation rate in the upper 400 m, an environment supporting mixing levels of $K_\rho \cong 5\times10^{-5}\ \mathrm{m^2\ s^{-1}}$. Deeper in the water column, mixing intensifies dramatically and (46) is found to underestimate the dissipation proxies by up to 2 orders of magnitude.

Klymak et al. [2010] use the disparity between observed and predicted dissipation to motivate the development of a simple parameterization for tidal mixing associated with knife-edge mid-ocean ridges that treats the dissipation as part of a deterministic wave-breaking process associated with small-vertical-scale internal tides having horizontal phase speeds C_{BC} slower than the barotropic tidal advection speed U_{BT}, i.e., $U_{BT}/C_{BC} > 1$. Here we argue that the large difference between observed and predicted dissipation may be understood as resulting from the application of the finescale parameterization to shear data with vertical scales smaller than the wave-breaking scale, i.e., $m \gg m_c$. As illustrated by Figure 2, this would be the result of taking a 4 m first-difference estimate of vertical shear in the lower part of the water column [see *Gargett*, 1990].

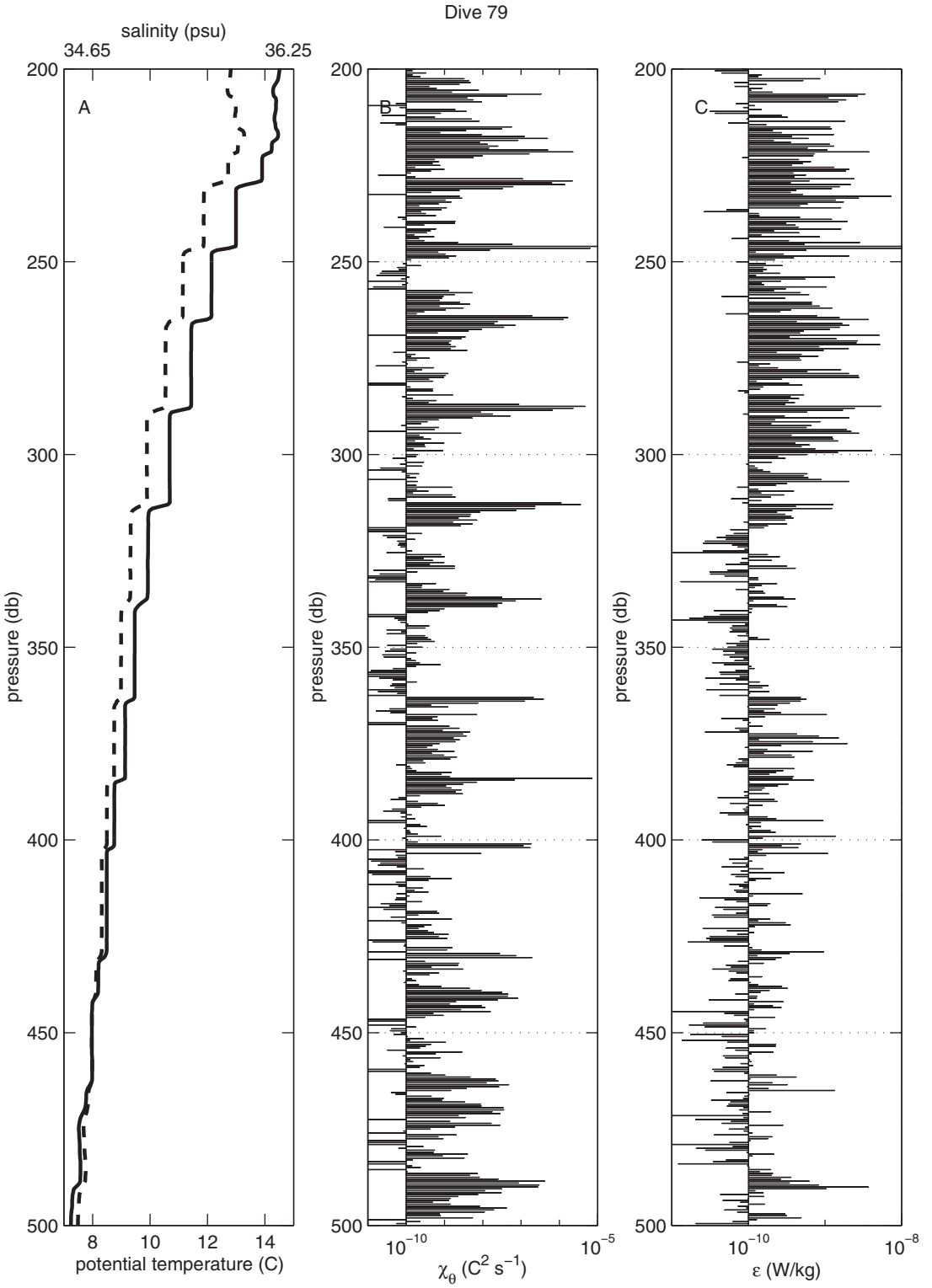

Figure 13. (a) Vertical profiles of potential temperature (solid) and salinity (dashed), (b) χ_θ, and (c) ϵ. This profile was selected because of the beautiful staircase structure in θ and S. It is atypical.

Consistent with this view, we note that the finescale parameterization (19) was used in a representation of tidal mixing associated with nominally subcritical mid-ocean ridge topographic roughness in *Polzin* [2004b]. In that study, the vertical wavelength corresponding to $U_{BT}/C_{BC} > 1$ plays a crucial role in the near-bottom

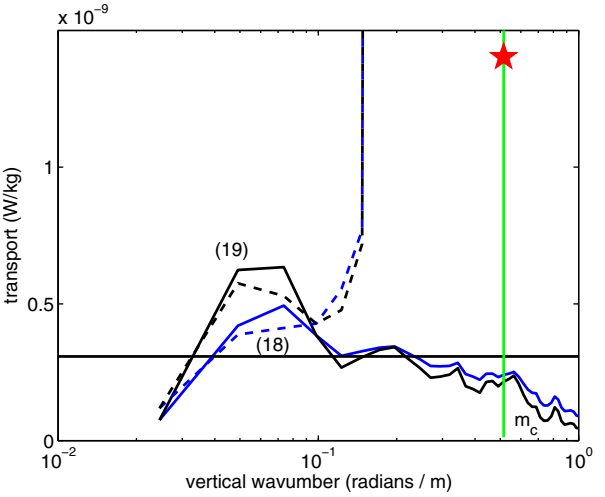

Figure 14. Transport estimates for SFtre2 using (18)—blue and (19)—black. Dashed traces use the observed spectra, solid traces use an estimate of the average spectral levels at low wave number deemed to be less contaminated be quasi-permanent finestructure. The cutoff m_c is represented as the green vertical line and $(1+R_f)$ times the observed dissipation is represented as the red symbol. The horizontal black line uses shear spectral levels averaged to m_c and the low wave number averaged estimate of shear-strain ratio. The finescale parameterization seriously underpredicts the estimate of the observed production rate. Profiles 28–80 from SFtre2, $R_\omega = 3$, $\epsilon = 12.2 \times 10^{-10}$ W/kg and $272 < p < 528$ db.

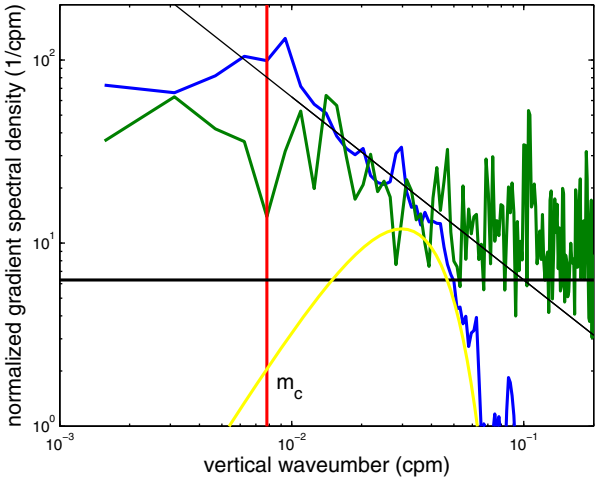

Figure 15. SOFine shear and strain spectra from selected sections (depths of [780−1420, 780−1420, 3520−4160, 3095 − 3735, 2825 − 3465, 770 − 1410, 1355 − 1995, 2000−2640, 2675−3315] m) of selected profiles (stations [6, 10, 31, 38, 42, 59, 61, 63, 65], respectively) that exhibit $F_r \geq O(0.1)$ and a tendency of the finescale parameterization to overpredict the observed dissipation (*Waterman et al.*, 2014). The shear spectrum is in blue, the strain in green, the nominal high wave number asymptote of the GM spectrum is represented by the horizontal black line, the LADCP noise spectrum is in yellow and the vertical cutoff 20 is given by the vertical red line. The thin black line represents an m_c/m roll-off.

parameterization of mixing associated with finescale baroclinic tides. The two opinions regarding the applicability of the finescale parameterization to the tidal mixing problem are clearly contradictory. We perceive that the issue lies in *Klymak et al.* [2008]'s application of the finescale parameterizations at wave numbers $m \gg m_c$.

A second example concerns data obtained about Monterey Canyon. *Kunze et al.* [2002] report a factor of 30 disparity between predictions based upon the finescale parameterization and observed dissipations reported in *Carter and Gregg* [2002]. A factor of 30 points to a robust discrepancy between prediction and observation. However, *Gregg et al.* [2005] report a processing error that leads to an order of magnitude bias of their dissipation rate estimates. We further note that *Kunze et al.* [2002] used 128 m transform lengths in their analysis. Since this is similar in magnitude to $2\pi/m_c$, we infer via (39) a tendency to underestimate the finescale parameterization production rate, and anticipate a further bias of a factor of 3 for the largest spectral levels in that analysis: it is unclear that the finescale parameterization production rate can be distinguished from the observed dissipation.

A third example is reported in *Polzin et al.* [1995] and comes from the steeply sloping flanks of Fieberling Guyot. In that example, the finescale Parameterization exhibited a slight (less than a factor of two) tendency to underpredict the observed dissipation ratel. Those authors attribute the underestimate to the biased estimate of ϕ, section 3.2.1.

We expect that the transfers upon which the finescale parameterization is predicated can be short circuited by boundary conditions. The degree to which this happens, though, is an open question.

5.6. Further Subtleties in the Physical Interpretation of Finescale Parameterization Results

Even in oceanic regimes in which the physics of turbulent production implicit in finescale parameterizations hold to an adequate degree, the outcome of the parameterizations can be very sensitive to rather subtle differences in formulation and implementation choices. An illustration of sensitivity to a relatively modest simplification of (40) is provided by the recent work of *Silverthorne and Toole* [2009]. These authors approximate the GM formula (27) as

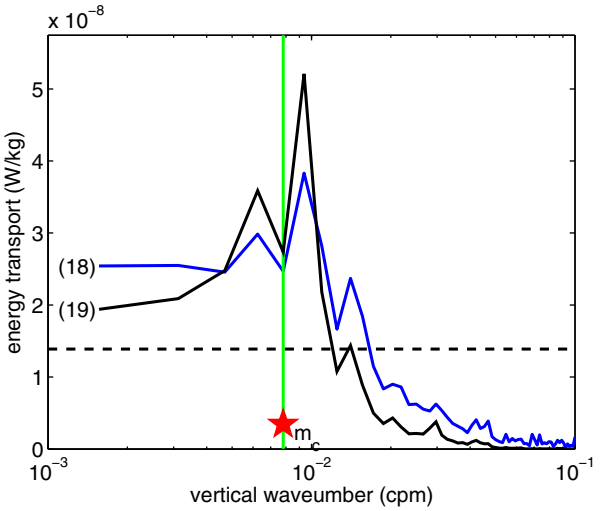

Figure 16. Transport estimates for SOFine using (18)—blue and (19)—black. The cutoff m_c is represented as a green vertical line and $(1+R_f)$ times the observed dissipation is represented as the red symbol. The dashed horizontal black line uses shear spectral levels averaged to m_c and a similarly averaged estimate of shear-strain ratio. The finescale parameterization seriously overpredicts the estimate of the observed production rate.

$$\epsilon = 7\times10^{-10}\frac{N^2}{N_o^2}\frac{E^2}{E_o^2}\ [\mathrm{W\ kg^{-1}}], \qquad (47)$$

and replace $\hat{E}$ by an estimate of near-inertial kinetic energy and E_o by an estimate of the average summertime near-inertial kinetic energy. Starting from the GM formula, they neglect the aspect ratio (ϕ) dependence of the rate of nonlinear energy cascading through the vertical wave number domain (26) and changes in the bandwidth (m_o) that appear in (27).

The above simplifications lead to results that are quantitatively and qualitatively different from those obtained using expression (40). To demonstrate this point, consider the average summer and winter spectra from the same data set presented in *Polzin and Lvov* [2011], Figure 17. From these data, we estimate

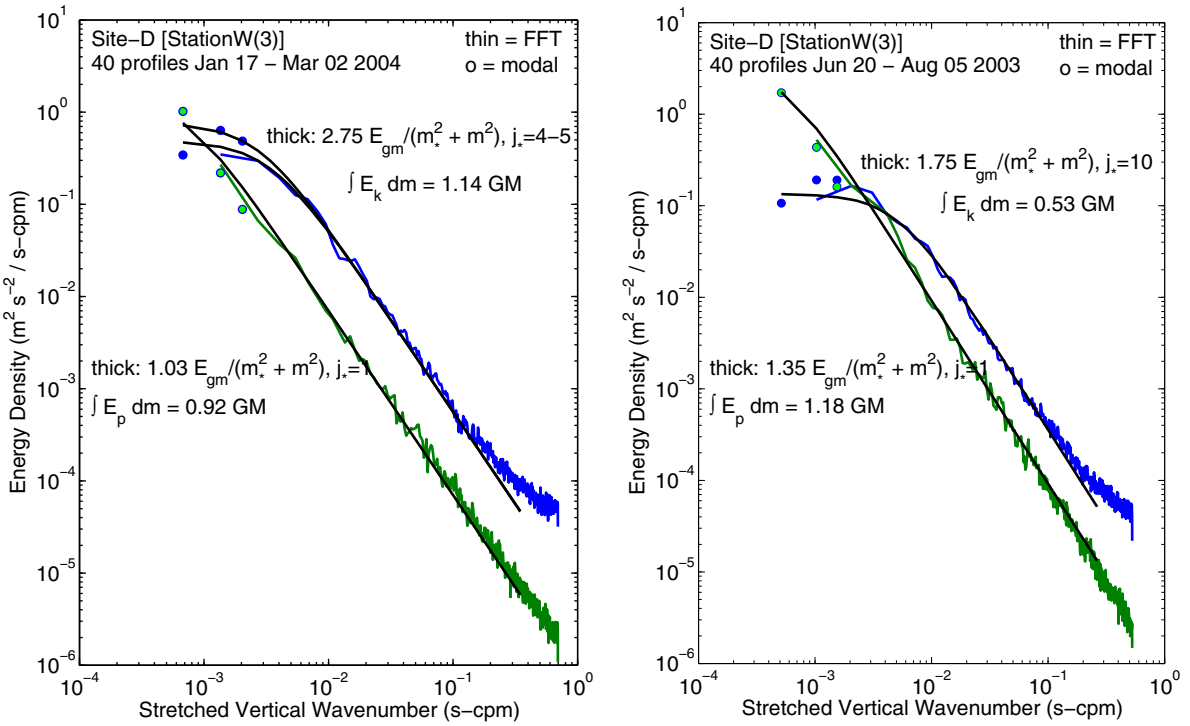

Figure 17. Site-D vertical wave number spectra of horizontal kinetic (blue) and potential (green) energy from *Polzin and Lvov* [2011]. Black lines represent fits of the GM76 spectrum with variable bandwidth j_*. Spectral estimates at the lowest wave number (enclosed circles) were made using a modal fit. Velocity and density profiles were obtained with a Moored Profiler. Information regarding the internal wavefield is returned by burst sampling 4 times using a 9.5 h sampling interval, then waiting 5 days before repeating. The spectrum presented here represents departures from the burst means. Departure from the curve fit at vertical wavelengths of 10 m and smaller is interpreted as noise.

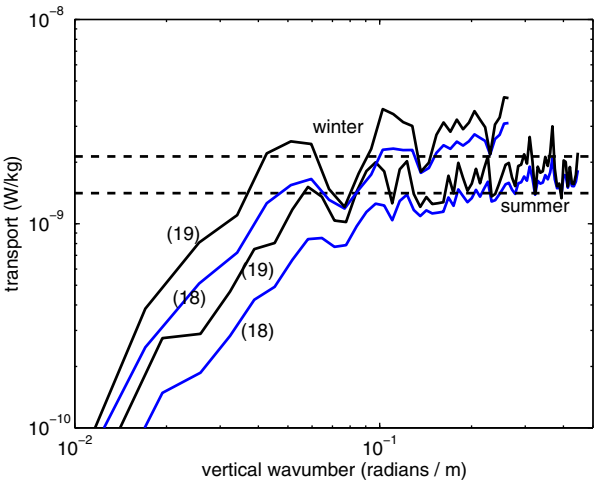

Figure 18. Transport estimates for SiteD using (18)—blue and (19)—black for both summer and winter time conditions. Spectra are truncated at m_c and the dashed horizontal lines use spectral levels averaged to m_c to estimate E and R_ω. Note that the finescale parameterization converges at high wave number. This is characteristic of spectra consistent with the GM spectral model.

$$\text{wintertime}: R_\omega = 8, \hat{E} = 2.75, \int E_k dm = 1.14\text{GM}$$

$$\text{summertime}: R_\omega = 4, \hat{E} = 1.75, \int E_k dm = 0.53\text{GM}$$

Using (40), we infer little seasonal difference and higher rates of dissipation and mixing ($K_\rho = 1.3\times10^{-5}$ (summer), 1.8×10^{-5} (winter), compared to *Silverthorne and Toole* [2009]'s nominal summer time value of $K_\rho = 0.5\times10^{-5}$ (summer) and a seasonal cycle of $O[E_k(\text{winter})/E_k(\text{summer})]^2 \cong 4$, Figure 18. The extent to which this impacts their conclusions regarding the spatial locality of the internal wave energy balance is unclear.

Use of the finescale parameterization here supports an interpretation that the larger bandwidth (m_o) and smaller shear-to-strain ratios (R_ω) in summer are indicative of an energetic pathway from near-inertial frequencies to the internal wave continuum. We find this to be a useful addition to the study of near-inertial energetics by *Silverthorne and Toole* [2009] that is not revealed in their analysis.

5.7. Recapitulation

The finescale parameterization is an attempt to represent the coupling of high-frequency internal waves to the vertical shear of near-inertial oscillations as a net transport of energy to smaller vertical wavelength and ultimately to wave breaking scales. The intent is to capture the dynamics within a finite amplitude and potentially strongly nonlinear parameter regime. This parameter space is bounded by vertical wave numbers $m \leq m_c$, with higher vertical wave numbers occupying an even more strongly nonlinear and less wave-like parameter regime. At wave numbers $m \leq m_c$, nonlinear transports compete with wave-mean interactions, and these wave-mean interactions can dominate nonlinear transports, especially at larger ($m \ll m_c$) vertical scales. Finally, there is an issue of contamination by nonwave variability. Biases can arise in many ways:

1. If the finescale parameterization is applied to vertical wave numbers larger than m_c, an underestimate of the dissipation rate is obtained. This is clearly seen in Figure 9 and impacts the conclusions of *Kunze et al.* [2002] and *Klymak et al.* [2008].

2. The finescale parameterization translates nonwhite gradient spectra as having spectral transports that are a function of vertical wave number, Figure 2. The most robust estimate is obtained at m_c, just prior to the dynamical transition to the wave-breaking regime noted above. Nonwhite gradient spectra are likely harbingers of additional physics such as wave-mean interactions (SOFine) or the PSI decay of a bandwidth limited internal tide (NATRE). Even if $F(m)$ is evaluated at m_c, significant biases are possible, as in SOFine.

3. Near-boundary regions are problematic for the finescale parameterization. The parameterization does not capture nonwave stresses and boundary conditions that inject significant shear at wave numbers $m > m_c$ short circuit the downscale energy transfers that the parameterization is founded upon. The height of such near-boundary regions is ill-defined. Revisiting *Kunze et al.* [2002] and *Klymak et al.* [2008] with the intent of minimizing potential biases could provide further insight.

The finescale parameterization interprets the shear-strain ratio as a biased estimate of a mean aspect ratio. Strain estimates can be significantly contaminated by nonwave finestructure associated with thermocline scarring (a general concern illustrated here with the NATRE data set) or double diffusion (in special regions, illustrated here with SFTRE and the CSALT data set presented in *Gregg et al.* [2003]), with contamination

increasing with decreasing vertical scale. The later case has the additional complication of diffusive buoyancy fluxes significantly altering the relationship between shear production $\mathcal{P}$ and dissipation ϵ, section 2.2.

6. Summary and Discussion

6.1. Summary

In this article, the extensive internal wave theoretical literature and the authors' own experiences have been drawn upon to clarify the physical basis of, define an implementation procedure for and identify the potential biases of finescale parameterizations of turbulent dissipation by internal wave breaking. The parameterizations are based on two key assumptions, namely: (i) that the production of turbulent energy at small scales is the end result of a downscale energy transfer driven by nonlinear internal wave-wave interactions, evaluated at a vertical wave number close to that of the wave breaking scale; and (ii) that a stationary turbulent energy balance exists in which production is matched by dissipation and a buoyancy flux in fixed proportions. Nonlinearities in the equation of state and double diffusion are neglected in this balance.

The finescale parameterization is a flux representation of nonlinear spectral energy transports across the vertical wave number domain. It seeks to characterize transports at vertical wavelengths $\lambda_v = 1/m_c$, where m_c (20) represents a high-wave number transition to a regime of strongly nonlinear dynamics. At smaller scales, energy can be transported by other mechanisms, such as shear instabilities, directly to turbulent production scales. The finescale parameterization, however, is not a generic wave-wave interaction closure. Its representation of energy flow through the vertical wave number domain is distinct from that associated with weakly nonlinear resonant interactions in the internal wavefield, such as the parametric subharmonic instability. Similarly, it does not capture the downscale energy transports and subsequent turbulent mixing linked to boundary layer physics or hydraulic jumps, both of which are germane to highly sheared flows in constrained passages [*Polzin et al*., 1996b; K. L. Polzin et al., Ekman layers and boundary mixing in the Orkney Passage Outflow, manuscript in preparation, 2014].

Even for internal wavefields in which the representation of spectral energy transports implicit in finescale parameterizations provides a good description of the effects of wave-wave interactions, nonlinearity is not the only physical mechanism that may result in spectral transports. Linear wave propagation in spatially inhomogeneous environments (i.e., buoyancy scaling and wave-mean interactions) leads to transfers of energy in the spectral domain that are not accounted for in the finescale parameterization. Scale transformations by scattering and reflection or generation at boundaries can inject energy at vertical wavelengths smaller than $1/m_c$ and bypass the nonlinear transfer process. These all have respective representations in a radiation balance scheme, but are absent from the finescale parameterizations. Our expectation is that if wave-mean interactions are sufficiently weak, i.e. $\bar{U}_z/N < 1/8$, then the finescale parameterizations will capture the spectral transport of energy at m_c when sufficiently far from boundaries (i.e., a distance greater than $1/2\pi m_c$).

The finescale parameterizations are formulated by reference to the Garrett and Munk (GM) internal wave spectrum, for which the high vertical wave number asymptote [$E(m) \propto m^{-2}$] represents an inertial subrange. Spectral energy transports through vertical wave number space are proportional to the expected value of the aspect ratio assuming a continuous distribution

$$<\frac{k_h}{m}> = \int_f^N \left(\frac{\omega^2 - f^2}{N^2 - \omega^2}\right)^{1/2} E(\omega) d\omega.$$

In the context of vertical profile data, the expected value of the aspect ratio is inferred assuming a single frequency,

$$<\frac{k_h}{m}> \cong \frac{f}{N}\left[\frac{2E_p(m)}{E_k(m) - E_p(m)}\right]^{1/2}.$$

The single frequency formula is a *biased* estimator of a continuous distribution, tending to underestimate (overestimate) the expected value of the aspect ratio if the frequency spectrum is whiter (redder) than GM. The bias can be as large as a factor of 2–3. Departures from the GM model in the vertical wave number

domain are handled by writing the spectral energy transports in such a way that non-GM vertical wave number spectra are relaxed to be consistent with GM. This formula involves two different moments of the vertical spectrum: $mE(m)\int_0^m 2m'^2\,E(m')dm'$. These moments are generally rendered as $2[m^2E(m)]^2$ and estimated by averaging $m^2E(m)$ in vertical wave number and squaring the result. While no approximation is required if the shear spectrum is white, the method otherwise returns a biased estimate. Thus, even with perfect data, the commonly used finescale parameterization formulae return biased estimates of spectral energy transports for non-GM vertical wave number spectra. That bias can be approximately a factor of 2 (34). However, if the covariability between the redder vertical wave number spectra and whiter frequency spectra noted by *Polzin and Lvov* [2011] is a general trend, the bias in vertical wave number will tend to cancel the bias in the frequency domain.

Generally, finescale parameterization physics have the greatest chance of dominating other transport terms near wave-breaking vertical scales ($m > m_c$), and thus should ideally be applied to $m \leq m_c$. However, the instrumentation most commonly used to estimate vertical profiles of horizontal velocity does not adequately resolve $1/m_c$. In these cases, reliance on finestructure observations of suboptimal resolution (i.e., on a vertical wave number $m \ll m_c$) exposes parameterization results to a wide range of additional possible sources of bias. These include an overestimation of ϵ in regions where PSI is common (approximately a factor of 2, Figure 10b, section 5.2, and biases of either sense in areas of intense wave-mean flow interactions [see e.g., *Waterman et al.*, 2013, where biases of up to an order of magnitude were found in the Antarctic Circumpolar Current].

Biases in results of the parameterizations may also be introduced by deficiencies in their implementation and by failures to recognize instrumental artifacts. Amongst the former, seemingly minor errors in the estimation of the buoyancy frequency may result in biases of an order of magnitude in the turbulent dissipation rate; contamination of strain estimates by quasi-permanent finestructure can lead to similarly substantial overestimation of ϵ; and the calculation of shear and strain over different bandwidths can be conducive to significant biases (typically of a factor of 2) for internal wavefields with nonwhite shear and strain spectra. The most notable instrument-related sources of bias include the contamination of density finestructure observations by characteristic mismatches between CTD sensor response times and by entrainment of water within the CTD rosette, and the introduction of spurious signals to LADCP and EM current meter velocity finestructure observations by measurement noise and processing procedures. Both of these may cause considerable (by up to an order of magnitude) overestimation of ϵ if not identified and excluded from the strain and shear variance calculations implicit in finescale parameterizations.

6.2. Discussion

The increased application of finescale parameterizations over the last decade has tantalized the observational and numerical modeling communities with the prospect of subbasin to global-scale estimates of the spatial distribution of diapycnal diffusivity (κ_ρ), something not imaginable from direct (microstructure) estimates of ϵ. It was widely envisaged at the outset of that period that such indirect estimates of κ_ρ could constrain observation-based inverse models of the large-scale ocean circulation, and inform the development of physically based parameterizations of small-scale mixing in numerical models. While these expectations may seem to be challenged by the range of bias-inducing assumptions implicit in finescale parameterization physics and compromises incurred in their application, we suggest that they can be realized with awareness of the causes of the biases and the adoption of implementation practices that minimize those biases. The reason is simple: given the above discussion, the biases associated with results of carefully implemented finescale parameterizations should be substantially less than an order of magnitude over much of the ocean. Many of the large-scale ocean circulation problems, in contrast, are associated with plausible ranges in ϵ or κ_ρ spanning typically an order of magnitude. Examples are provided by the order-of-magnitude range in Southern Ocean interior diapycnal diffusivity estimates yielded by the inverse models of *Ganachaud and Wunsch* [2000], *Sloyan and Rintoul* [2001], *Lumpkin and Speer* [2007], and *Zika et al.* [2009], as well as by the order-of-magnitude range in basin-averaged turbulent dissipation implied by existing plausible inverse estimates of the meridional overturning of the deep Indian Ocean [*Huussen et al.*, 2012].

As way of illustrating of this point, consider the contrasting findings of *Sloyan* [2006] and *Huussen et al.* [2012] in the context of comparisons between basin-averaged turbulent diapycnal mixing rates inferred from the application of finescale parameterizations and from large-scale water mass budgets. *Sloyan* [2006] found a good correspondence between the two sets of estimates of diapycnal mixing rates in the Perth

Basin, an area partially enclosed by topography in which deep water has to upwell diapycnally in order to exit the basin. From that result addressing the southwest abyssal Indian Ocean, she concluded that internal wave breaking was the dominant process in driving diapycnal water mass transformations in the basin. In contrast, *Huussen et al*. [2012] noted that the area-averaged rate of diapycnal upwelling diagnosed from finescale techniques was significantly lower (typically by a factor of 5–10) than implied by existing inverse estimates of the deep overturning circulation over the Indian Ocean north 30S. Combined with a range of ancillary evidence, this finding led those authors to conclude that the deep Indian Ocean overturning is predominantly sustained by near-boundary processes.

There is room for both studies to be correct in their assessments. Our short list for resolving these disparate conclusions contains (i) the possibility of spatial/temporal sampling bias in station data utilized in *Huussen et al*. [2012] with respect to hot spots of wave driven turbulent dissipation (section 4.1.3) and (ii) the possibility that mixing associated with bottom boundary layer physics and highly sheared flows in constrained passages can play a dominant role in basin scale mass and buoyancy budgets. These issues are highly context dependent, potentially much more so than, for example, the possible short-circuiting of the downscale energy transfer by boundary conditions, section 5.5.

We note other examples where the finescale parameterization has been employed to address large-scale circulation issues. K. L. Polzin et al. (Ekman layers and boundary mixing in the Orkney Passage Outflow, manuscript in preparation, 2014) employ both finescale parameterizations and a Thorpe-scale analysis to examine diapycnal transformations experienced by the Antarctic Bottom Water (AABW) entering the Scotia Sea through the Orkney Passage [*Heywood et al*., 2002]. They find internal wave breaking is only of secondary importance to the deep buoyancy budget of that basin. *Naveira Garabato et al*. [2013] have conducted, to our knowledge, the only attempt to date to incorporate diapycnal mixing rates estimated from finescale parameterizations into an inverse model of the large-scale ocean circulation. Their study of the Southern Ocean showed that such diapycnal mixing estimates can provide a useful constraint on the circulation diagnosed by the inversion. A significant result of that work, which the finescale diagnostics contributed to shape, is the inference that a total of 15 Sv of AABW are exported from the subpolar gyres to the midlatitude Southern Ocean and undergo significant diapycnal upwelling there. A considerably weaker lower overturning cell had been suggested by most preceding studies, e.g., *Lumpkin and Speer* [2007] estimated 8 Sv of circumpolar AABW production, which appears difficult to reconcile with the direct measurement of 6 Sv of AABW through the Orkney Passage alone [*Garabato et al*., 2002].

To conclude, we wish to encourage the physical oceanographic community to exploit finescale parameterizations in addressing problems related to the (subbasin to global scale) spatiotemporal distribution of turbulent dissipation and diapycnal mixing, to parameterization of mixing processes in numerical models and, when used in conjunction with microstructure measurements, to the study of the dominant dynamical balances in the internal wavefield. If applied and interpreted carefully, the parameterizations have much valuable information to contribute to these important issues, as illustrated by a range of examples outlined throughout this article. We hope that this review will help to dispel any reservations that some sectors of the community may have about the parameterizations' usefulness, and reignite enthusiasm for their application to finestructure observations.

Appendix A: Dynamical Consistency of the Energy Balance (13)

The intent here is to demonstrate that the energy balance scheme (13) represents a dynamically consistent scenario. Our starting place is the action balance

$$\frac{\partial \mathcal{N}}{\partial t} + \nabla_{\mathbf{p}} \sigma(\mathbf{p}, \mathbf{r}) \cdot \nabla_{\mathbf{r}} \mathcal{N} - \nabla_{\mathbf{r}} \sigma(\mathbf{p}, \mathbf{r}) \cdot \nabla_{\mathbf{p}} \mathcal{N} = 0 \tag{A1}$$

and its equivalent flux form

$$\frac{\partial \mathcal{N}}{\partial t} + \nabla_{\mathbf{r}} \cdot [\nabla_{\mathbf{p}} \sigma(\mathbf{p}, \mathbf{r})] \mathcal{N} - \nabla_{\mathbf{p}} \cdot [\nabla_{\mathbf{r}} \sigma(\mathbf{p}, \mathbf{r})] \mathcal{N} = 0.$$

This action balance can be systematically derived for a broad class of Hamiltonian systems [*Gershgorin et al*., 2009] with only an assumption of a scale separation. Spatial localization is addressed using a windowing

(wavelet) procedure that assumes a wave packet to be sufficiently peaked to define a local wave number. Here $\sigma(\mathbf{p},\mathbf{r})$ is an Eulerian phase function associated with the quadratic terms of the Hamiltonian structure and gradients of the Eulerian phase represent the characteristics of (A1). The action balance (A1) states that action density $\mathcal{N}$ is conserved along these characteristics in the six-dimensional spatial-spectral domain. In the small amplitude limit, the familiar relations $\sigma(\mathbf{p},\mathbf{r})=\omega+\mathbf{p}\cdot\overline{\mathbf{u}}$; $\nabla_{\mathbf{p}}\sigma(\mathbf{p},\mathbf{r})=\mathbf{C_g}+\overline{\mathbf{u}}$ and the ray tracing relations $\nabla_{\mathbf{r}}\sigma(\mathbf{p},\mathbf{r})\equiv\mathcal{R}$ are recovered. Application of (A1) to finite amplitude wave packets requires a transformation to the prerequisite Hamiltonian form. Thus, for example, extension to solitary wave propagation with an amplitude dependent intrinsic frequency requires further consideration.

We proceed by integrating over the spatial domain and invoking "periodic in space" boundary conditions to obtain

$$\frac{\partial\mathcal{A}(\mathbf{p})}{\partial t}+\nabla_{\mathbf{p}}\cdot[\mathbf{p}\mathcal{A}]=0 \tag{A2}$$

with

$$\mathcal{A}(\mathbf{p})=\int\mathcal{N}(\mathbf{p},\mathbf{r})d\mathbf{r}.$$

Rather than deriving a diffusive approximation to (A2) as in *Galtier et al*. [2001] we deal with (A2) directly. We first transform to a horizontal wave number magnitude k_h, horizontal azimuth ϕ coordinate system and average over horizontal azimuth:

$$\frac{\partial\mathcal{A}(k_h,m)}{\partial t}+\frac{\partial}{\partial k_h}[\dot{k}_h\mathcal{A}]+\frac{\dot{k}_h}{k_h}\mathcal{A}+\frac{\partial}{\partial m}[\dot{m}\mathcal{A}]=0. \tag{A3}$$

We then average over many wave packets and define the average action transports in terms of energy transports Q:

$$\langle\dot{k}_h\mathcal{A}\rangle\equiv Q^{k_h}/\omega,$$
$$\langle\dot{m}\mathcal{A}\rangle\equiv Q^{m}/\omega.$$

Application of the chain rule returns

$$\frac{\partial E(k_h,m)}{\partial t}+\frac{\partial}{\partial k_h}Q^{k_h}+\frac{\partial}{\partial m}Q^{m}=-\frac{Q^m}{m} \tag{A4}$$

Following the rules defined in (16) and using the GM76 dependence of $E(k_h,m)\propto 1/mk_h^2$, the energy transport in the vertical wave number domain is

$$Q^m=\langle\dot{m}E(\alpha,m)\rangle=\langle\dot{m}\rangle\langle E(\alpha,m)\rangle\propto m^0k_h^{-1},$$

independent of m. Thus, $\partial_m Q^m=0$ and a stationary state requires

$$\frac{\partial}{\partial k_h}Q^{k_h}=-\frac{Q^m}{m}. \tag{A5}$$

A general solution to (A5) is

$$Q^{k_h}=\frac{k_h}{m}\ln\left(\frac{m}{k_h}\right)Q^m+I(m).$$

The term $I(m)$ is an integration constant and determined by boundary conditions. We choose to apply the boundary conditions in the frequency domain and rotate the flux vector (Q^{k_h},Q^m) into a system aligned along and across frequency isopleths:

$$[Q^{\perp};Q^{\parallel}] \cong \left[Q^m \frac{k_h}{m}\left(\ln\frac{m}{k_h}-1\right)+I(m);Q^m\right].$$

Making the choice of a no-flux boundary condition at $\omega=N$ returns

$$[Q^{\perp};Q^{\parallel}] \cong \left[Q^m \frac{k_h}{m}\ln\left(\frac{m}{k_h}\right);Q^m\right]. \tag{A6}$$

Treating the vector **Q** as a flux density and transforming from (k_h,m) to (ω,m) coordinates finally provides

$$[Q^{\omega};Q^m] \propto \left[\ln\left(\frac{N}{\omega}\right);\frac{1}{\omega}\right], \tag{A7}$$

i.e., the transport of energy through the frequency domain is to higher frequency and is a logarithmic correction away from being independent of frequency. We furthermore conclude that (13) is consistent with the action conservation statement (A1), at least in the small amplitude and scale separated limits in which (A1) was derived. Whether (A1) is germane to the finite amplitude and likely strongly nonlinear parameter regime of the oceanic internal wavefield has yet to be seen.

Acknowledgments

K.L.P.'s salary support for this analysis was provided by Woods Hole Oceanographic Institution bridge support funds and NSF grant OCE-0926848. A.C.N.G. was supported by a NERC Advanced Research Fellowship (NE/C517633/1), T.N.H. by a National Oceanography Centre, Southampton PhD studentship, B.M.S. by the Australian Climate Change Science Program and CSIRO Wealth from Ocean National Research Flagship, and S.W. by Australian Research Council grants DE120102927 and CE110001028.

References

Alford, M. H., J. A. MacKinnon, Z. Zhao, R. Pinkel, J. Klymak, and T. Peacock (2007), Internal waves across the Pacific, *Geophys. Res. Lett.*, *34*, L24601, doi:10.1029/2007GL031566.

Bray, N. A., and N. P. Fofonoff (1983), Available potential energy for MODE eddies, *J. Phys. Oceanogr.*, *11*, 30–46.

Brink, K. H. (1995), Tidal and lower frequency currents above Fieberling Guyot, *J. Geophys. Res.*, *100*, 10,817–10,832.

Carter, G. S., and M. C. Gregg (2002), Intense, variable mixing near the head of Monterey Submarine Canyon, *J. Phys. Oceanogr.*, *32*, 3145–3165.

Chen, C.-T., and F. M. Millero (1977), Speed of sound in seawater at high pressures, *J. Atmos. Sci.*, *62*, 1129–1135.

Daae, K. L., I. Fer, and E. P. Abrahamsen (2009), Mixing on the continental slope of the southern Weddell Sea, *J. Geophys. Res.*, *114*, C09018, doi:10.1029/2008JC005259.

Dillon, T. M., and M. M. Park (1987), The available potential energy of overturns as indicator of mixing in the seasonal thermocline, *J. Geophys. Res.*, *92*, 5345–5353.

Doherty, K. W., D. E. Frye, S. P. Liberatore, and J. M. Toole (1999), A moored profiler instrument, *J. Atmos. Oceanic Technol.*, *16*, 1816–1829.

Duda, T. F., and C. S. Cox (1989), Vertical wavenumber spectra of velocity and shear at small internal wave scales, *J. Geophys. Res.*, *94*, 939–950.

Eriksen, C. C. (1985), Implications of ocean bottom reflection for internal wave spectra and mixing, *J. Phys. Oceanogr.*, *15*, 1145–1156.

Eriksen, C. C. (1998), Internal wave reflection and mixing at Fieberling Guyot, *J. Geophys. Res.*, *103*, 2977–2994.

Fer, I., R. Skogseth, and F. Geyer (2010), Internal waves and mixing in the marginal ice zone near Yermak Plateau, *J. Phys. Oceanogr.*, *40*, 1613–1630.

Ferron, B., H. Mercier, K. Speer, A. Gargett, and K. Polzin (1998), Mixing in the Romanche fracture zone, *J. Phys. Oceanogr.*, *28*, 1929–1945.

Fischer, J., and M. Visbeck (1993), Deep velocity profiling with self-contained ADCPs, *J. Atmos. Oceanic Technol.*, *10*, 764–773.

Flatté, S. M., F. S. Henyey, and J. A. Wright (1985), Eikonal calculations of short-wavelength internal wave spectra, *J. Geophys. Res.*, *90*, 7265–7272.

Galtier, S., S. V. Nazarenko, and A. C. Newell (2001), Nonlocal MHD turbulence, *Physica D*, *152–153*, 646–652.

Ganachaud, A., and C. Wunsch (2000), Improved estimates of global ocean circulation, heat transport and mixing from hydrographic data, *Nature*, *408*, 453–457.

Garabato, A. C. N., E. L. McDonogh, D. P. Stevens, K. J. Heywood, and R. J. Sanders (2002), On the export of Antarctic bottom water from the Weddell Sea, *Deep Sea Res., Part II*, *49*, 4715–4742.

Garabato, A. C. N., K. L. Polzin, B. A. King, K. J. Heywood, and M. Visbeck (2004a), Widespread intense turbulent mixing in the Southern Ocean, *Science*, *303*, 210–213.

Garabato, A. C. N., K. I. C. Oliver, A. J. Watson, and M.-J. Messias (2004b), Turbulent diapycnal mixing in the Nordic Seas, *J. Geophys. Res.*, *109*, C12010, doi:10.1029/2004JC002411.

Garabato, A. C. N., A. P. Williams, and S. Bacon (2013), The three-dimensional overturning circulation of the Southern Ocean during the WOCE era, *Prog. Oceanogr.*, *120*, 41–78, doi:10.1016/j.pocean.2013. 07.018.

Gargett, A. E. (1990), Do we really know how to scale the turbulent kinetic energy rate ϵ due to breaking of oceanic internal waves?, *J. Geophys. Res.*, *95*, 15,971–15,974.

Gargett, A. E., P. J. Hendricks, T. B. Sanford, T. R. Osborn, and A. J. Williams (1981), A composite spectrum of vertical shear in the ocean, *J. Phys. Oceanogr.*, *11*, 1258–1271.

Garrett, C. J. R., and W. H. Munk (1975), Space-timescales of internal waves. A progress report, *J. Geophys. Res.*, *80*, 291–297.

Gershgorin, B., Y. V. Lvov, and S. Nazarenko (2009), Canonical Hamiltonians for waves in inhomogeneous media, *J. Math. Phys.*, *50*, 013527, doi:10.1063/1.3054275.

Gregg, M. C. (1989), Scaling turbulent dissipation in the thermocline, *J. Geophys. Res.*, *94*, 9686–9698.

Gregg, M. C., and E. Kunze (1991), Shear and strain in Santa Monica Basin, *J. Geophys. Res.*, *96*, 16,709–17,719.

Gregg, M. C., D. P. Winkel, and T. B. Sanford (1993), Varieties of fully resolved spectra of vertical shear, *J. Phys. Oceanogr.*, *23*, 124–141.

Gregg, M. C., T. B. Sanford, and D. P. Winkel (2003), Reduced mixing from the breaking of internal waves in equatorial waters, *Nature*, *422*, 513–515.

Gregg, M. C., G. S. Carter, and E. Kunze (2005), Corrigendum, *J. Phys. Oceanogr.*, *35*, 1712–1715.
Henyey, F. S., J. A. Wright, and S. M. Flatté (1986), Energy and action flow through the internal wave field: An eikonal approach, *J. Geophys. Res.*, *91*, 8487–8495.
Heywood, K. J., A. C. N. Garabato, and D. P. Stevens (2002), High mixing rates in the abyssal Southern Ocean, *Science*, *415*, 1011–1014.
Horne, E. P. W., and J. M. Toole (1980), Sensor response mismatches and lag correction techniques for temperature-salinity profilers, *J. Phys. Oceanogr.*, *10*, 1122–1130.
Huussen, T., A. C. N. Garabato, H. L. Bryden, and E. L. McDonagh (2012), Is the deep Indian Ocean MOC sustained by breaking internal waves?, *J. Geophys. Res.*, *117*, C08024, doi:10.1029/2012JC008236.
Iudicone, D., G. Madec, and T. J. McDougall (2008), Watermass transformations in a neutral density framework and the key role of light penetration, *J. Phys. Oceanogr.*, *38*, 1357–1376.
Jackett, D. R., and T. J. McDougall (1997), A neutral density variable for the world's oceans, *J. Phys. Oceanogr.*, *27*, 237–263.
Klymak, J. M., and J. N. Moum (2007a), Oceanic isopycnal slope spectra. Part I: Internal waves, *J. Phys. Oceanogr.*, *37*, 1215–1231.
Klymak, J. M., and J. N. Moum (2007b), Oceanic isopycnal slope spectra. Part II: Turbulence, *J. Phys. Oceanogr.*, *37*, 1232–1245.
Klymak, J. M., R. Pinkel, and L. Rainville (2008), Direct breaking of the internal tide near topography: Kaena Ridge, Hawaii, *J. Phys. Oceanogr.*, *38*, 380–399.
Klymak, J. M., S. Legg, and R. Pinkel (2010), A simple parameterization of turbulent mixing near supercritical topography, *J. Phys. Oceanogr.*, *40*, 2059–2074.
Kunze, E. (1985), Near-inertial wave propagation in geostrophic shear, *J. Phys. Oceanogr.*, *15*, 544–565.
Kunze, E., and T. B. Sanford (1993), Sub-mesoscale dynamics near a seamount. Part I: Measurements of Ertel vorticity, *J. Phys. Oceanogr.*, *23*, 2567–2588.
Kunze, E., and T. B. Sanford (1996), Abyssal mixing: Where it is not, *J. Phys. Oceanogr.*, *26*, 2286–2296.
Kunze, E., A. J. Williams, and M. G. Briscoe (1990), Interpreting shear and strain finestructure from a neutrally buoyant float, *J. Geophys. Res.*, *95*, 18,111–18,126.
Kunze, E., M. A. Kennelly, and T. B. Sanford (1992), The depth dependence of shear finestructure of Point Arena and near Pioneer Seamount, *J. Phys. Oceanogr.*, *16*, 29–41.
Kunze, E., L. K. Rosenfeld, G. S. Carter, and M. C. Gregg (2002), Internal waves in Monterey Submarine Canyon, *J. Phys. Oceanogr.*, *32*, 1890–1913.
Kunze, E., E. Firing, J. M. Hummon, T. K. Chereskin, and A. M. Thurnherr (2006), Global abyssal mixing from lowered ADCP shear and CTD strain profiles, *J. Phys. Oceanogr.*, *36*, 1553–1576.
Lauderdale, J. M., S. Bacon, A. C. N. Garabato, and N. P. Holliday (2008), Intensified turbulent mixing in the boundary current system of southern Greenland, *Geophys. Res. Lett.*, *35*, L04611, doi:10.1029/2007GL0 32785.
Leaman, K. D. (1976), Observations on the vertical polarization and energy flux of near-inertial waves, *J. Phys. Oceanogr.*, *6*, 894–908.
Leaman, K. D., and T. B. Sanford (1975), Vertical energy propagation of inertial waves: A vector spectral analysis of velocity profiles, *J. Geophys. Res.*, *80*, 1975–1978.
Lueck, R. G. (1990), Thermal inertia of conductivity cells: Theory, *J. Atmos. Oceanic Technol.*, *7*, 741–755.
Lueck, R. G., and J. J. Picklo (1990), Thermal inertia of conductivity cells: Observations with a Sea-Bird cell, *J. Atmos. Oceanic Technol.*, *7*, 756–768.
Lueck, R. G., O. Hertzman, and T. R. Osborn (1977), The spectral response of thermistors, *Deep Sea Res.*, *24*, 951–970.
Lumpkin, R., and K. Speer (2007), Global ocean meridional overturning, *J. Phys. Oceanogr.*, *37*, 2550–2562.
MacKinnon, J. A., T. M. S. Johnston, and R. Pinkel (2008), Strong transport and mixing of deep water through the Southwest Indian Ridge, *Nat. Geosci.*, *1*, 755–758, doi:10.1037/ngeo340.
Mauritzen, C., K. L. Polzin, M. S. McCartney, R. C. Millard, and D. E. West-Mack (2002), Evidence in hydrography and density finestructure for enhanced vertical mixing over the Mid-Atlantic Ridge in the western Atlantic, *J. Geophys. Res.*, *107*(C10), 3147, doi:10.1029/2001JC001114.
McComas, C. H., and P. Müller (1981), Timescales of resonant interactions among oceanic internal waves, *J. Phys. Oceanogr.*, *11*, 139–147.
McDougall, T. J. (1987), Thermobaricity, cabbeling, and water-mass conversion, *J. Geophys. Res.*, *92*, 5448–5464.
Millard, R. C., W. B. Owens, and N. P. Fofonoff (1990), On the calculation of the Brunt-Väisälä frequency, *Deep Sea Res., Part A*, *37*, 167–181.
Moum, J. N. (1990), The quest for Kρ—Preliminary results from direct measurements of turbulent fluxes in the ocean, *J. Phys. Oceanogr.*, *20*, 180–184.
Müller, P., and N. Xu (1992), Scattering of oceanic internal gravity waves off random bottom topography, *J. Phys. Oceanogr.*, *22*, 7474–488.
Müller, P., G. Holloway, F. Henyey, and N. Pomphrey (1986), Nonlinear interactions among internal gravity waves, *Rev. Geophys.*, *24*, 493–536.
Nazarenko, S. (2011), Wave Turbulence, Springer, Berlin.
Palmer, M. D., A. C. N. Garabato, J. D. Stark, J. J.-M. Hirschi, and J. Marotzke (2007), The influence of diapycnal mixing on quasi-steady overturning states in the Indian Ocean, *J. Phys. Oceanogr.*, *27*, 2290–2304.
Park, Y.-H., J.-L. Fuda, I. Durand, and A. C. N. Garabato (2008), Internal tides and vertical mixing over the Kergulean Plateau, *Deep Sea Res., Part II*, *55*, 582–593.
Peltier, W. R., and C. P. Caulfield (2003), Mixing efficiency in stratified shear flows, *Annu. Rev. Fluid Mech.*, *35*, 135–167.
Plueddemann, A. J. (1992), Internal wave observations from the Arctic environmental drifting buoy, *J. Geophys. Res.*, *97*, 12,619–12,638.
Polzin, K. L. (1996), Statistics of the Richardson number: Mixing models and finestructure, *J. Phys. Oceanogr.*, *26*, 1409–1425.
Polzin, K. L. (2004a), A heuristic description of internal wave dynamics, *J. Phys. Oceanogr.*, *34*, 214–230.
Polzin, K. L. (2004b), Idealized solutions for the energy balance of the finescale internal wavefield, *J. Phys. Oceanogr.*, *34*, 231–246.
Polzin, K. L. (2008), Mesoscale eddy-internal wave coupling. I. Symmetry, wave capture and results from the mid-Ocean dynamics experiment, *J. Phys. Oceanogr.*, *38*, 2556–2574.
Polzin, K. L. (2009), An abyssal recipe, *Ocean Modell.*, *30*, 298–309.
Polzin, K. L., and R. Ferrari (2004), Isopycnal dispersion in NATRE, *J. Phys. Oceanogr.*, *34*, 247–257.
Polzin, K. L., and Y. L. Lvov (2011), Toward regional characterizations of the oceanic internal wavefield, *Rev. Geophys.*, *49*, RG4003, doi:10.1029/2010RG000329.
Polzin, K. L., J. M. Toole, and R. W. Schmitt (1995), Finescale parameterizations of turbulent dissipation, *J. Phys. Oceanogr.*, *25*, 306–328.
Polzin, K. L., N. S. Oakey, J. M. Toole, and R. W. Schmitt (1996a), Finestructure and microstructure characteristics across the northwest Atlantic Subtropical Front, *J. Geophys. Res.*, *101*, 14,111–14,121.
Polzin, K. L., K. Speer, J. M. Toole, and R. W. Schmitt (1996b), Mixing in the Romanche fracture zone, *Nature*, *380*, 54–57.

Polzin, K. L., E. Kunze, J. Hummon, and E. Firing (2002), The finescale response of lowered ADCP velocity profilers, *J. Atmos. Oceanic Technol.*, *19*, 205–224.
Polzin, K. L., E. Kunze, J. M. Toole, and R. W. Schmitt (2003), The partition of finescale energy into internal waves and subinertial motions, *J. Phys. Oceanogr.*, *33*, 234–238.
RDInstruments (1996), *Acoustic Doppler Current Profiler—Principles of Operation: A Practical Primer*, 54 pp.
Sanford, T. B. (1971), Motionally induced electric and magnetic fields in the sea, *J. Geophys. Res.*, *76*, 3476–3492.
Sanford, T. B. (1975), Observations of the vertical structure of internal waves, *J. Geophys. Res.*, *80*, 3861–3871.
Sanford, T. B., R. G. Drever, J. H. Dunlap, and E. A. D'Asaro (1982), Design, operation and performance of an expendable temperature and velocity profiler (XTVP), *Appl. Phys. Lab. Tech. Rep. 8110*, 83 pp., Univ. of Washington, Seattle.
Sanford, T. B., E. A. D'Asaro, E. Kunze, J. H. Dunlap, R. G. Drever, M. A. Kennelly, M. A. Prater, and M. S. Horgan (1993), An XCP users guide and reference manual, *Appl. Phys. Lab. Tech. Rep. APL-UW TR 9309*, 59 pp., Univ. of Washington, Seattle.
Schmitt, R. W. (1994), Double diffusion in Oceanography, *Annu. Rev. Fluid Mech.*, *26*, 255–285.
Schmitt, R. W., R. C. Millard, J. M. Toole, and W. D. Wellwood (2005a), A double-diffusive interface tank for dynamic response studies, *J. Mar. Res.*, *63*, 263–289.
Schmitt, R. W., J. R. Ledwell, E. T. Montgomery, K. L. Polzin, and J. M. Toole (2005b), Enhanced diapycnal mixing by salt fingers in the thermocline of the Tropical Atlantic, *Science*, *308*, 685–688.
Silverthorne, K. E., and J. M. Toole (2009), Seasonal kinetic energy variability of near-inertial motions, *J. Phys. Oceanogr.*, *39*, 1035–1049.
Sloyan, B. M. (2005), Spatial variability of mixing in the Southern Ocean, *Geophys. Res. Lett.*, *32*, L18603, doi:10.1029/2005GL023568.
Sloyan, B. M. (2006), Antarctic bottom and lower circumpolar deep water circulation in the eastern Indian Ocean, *J. Geophys. Res.*, *111*, C02006, doi:10.1029/2005JC003011.
Sloyan, B. M., and S. R. Rintoul (2001), The Southern Ocean limb of the global deep overturning circulation, *J. Phys. Oceanogr.*, *31*, 143–173.
Stevens, D., and V. O. Ivchenko (1997), The zonal momentum balance in an eddy-resolving general circulation model of the Southern Ocean, *Q. J. R. Meteorol. Soc.*, *123*, 929–951.
Stöber, U., M. Walter, C. Mertens, and M. Rhein (2008), Mixing estimates from hydrographic measurements in the Deep Western Boundary Current of the North Atlantic, *Deep Sea Res., Part I*, *55*, 721–736.
Theriault, K. B. (1986), Incoherent multibeam Doppler current profiler performance: Part I—Estimate variance, *IEEE J. Oceanic Eng.*, *11*, 7–15.
Thorpe, S. A. (1977), Turbulence and mixing in a Scottish Loch, *Philos. Trans. R. Soc. London A*, *286*, 125–181.
Thurnherr, A. M., and K. G. Speer (2003), Boundary mixing and topographic blocking on the Mid-Atlantic Ridge in the South Atlantic, *J. Phys. Oceanogr.*, *33*, 848–862.
Toole, J. M., K. W. Doherty, D. E. Frye, and R. C. Millard (1997), A wire-guided, free-fall system to facilitate ship-borne hydrographic profiling, *J. Atmos. Oceanic Technol.*, *14*, 667–675.
Visbeck, M. (2002), Deep velocity profiling using lowered Acoustic Doppler Current Profilers: Bottom track and inverse solution, *J. Atmos. Oceanic Technol.*, *19*, 794–807.
Walter, M., C. Mertens, and M. Rhein (2005), Mixing estimates from a large-scale hydrographic survey in the North Atlantic, *Geophys. Res. Lett.*, *32*, L13605, doi:10.1029/2005GL022471.
Waterman, S., A. C. N. Garabato, and K. L. Polzin (2013), Internal waves and turbulence in the Antarctic Circumpolar Current, *J. Phys. Oceanogr.*, *43*, 259–282.
Waterman, S., K. L. Polzin, A. C. Naveira Garabato, K. L. Sheen, and A. Forryan (2014), Suppression of internal wave breaking in the Antarctic Circumpolar Current near topography, *Journal of Physical Oceanography*, doi:10.1175/JPO-D-12-0154.1, in press.
Whalen, C. B., L. D. Talley, and J. A. MacKinnon (2012), Spatial and temporal variability of global ocean mixing inferred from ARGO profiles, *Geophys. Res. Lett.*, *39*, L18612, doi:10.1029/2012GL053196.
Winkel, D. P., M. C. Gregg, and T. B. Sanford (2002), Patterns of shear and turbulence across the Florida Current, *J. Phys. Oceanogr.*, *32*, 3269–3285.
Wu, L., Z. Jing, S. Riser, and M. Visbeck (2011), Seasonal and spatial variations of Southern Ocean diapycnal mixing from Argo profiling floats, *Nat. Geosci.*, *4*, 363–366, doi:10.1038/NGEO1156.
Wunsch, C., and R. Ferrari (2004), Vertical mixing, energy, and the general circulation of the oceans, *Annu. Rev. Fluid Mech.*, *36*, 281–314.
Zakharov, V. E., V. S. Lvov, and G. Falkovich (1992), *Kolmogorov Spectra of Turbulence*, 275 pp., Springer, Berlin.
Zika, J. D., B. M. Sloyan, and T. J. McDougall (2009), Diagnosing the Southern Ocean overturning from tracer fields, *J. Phys. Oceanogr.*, *39*, 2926–2940.